Protonic Transport Properties of Perovskite Heterostructures

A Thin Film Study

Erik E. P. Alsgaard

Supervisors:
Truls Norby, Reidar Haugsrud, Tor Bjørheim

Master Thesis
Materials Science for Energy and Nanotechnology
60 credits

Department of Chemistry
The Faculty of Mathematics and Natural Sciences

UNIVERSITY OF OSLO

[06 / 2021]

Protonic Transport Properties of Perovskite Heterostructures

A Thin Film Study

2021

Protonic Transport Properties of Perovskite Heterostructures

Erik E. P. Alsgaard

http://www.duo.uio.no/

Trykk: Reprosentralen, Universitetet i Oslo

Preface

This thesis represents part of the required work for the degree of Master of Science (M.Sc.) at the Department of Chemistry, The Faculty of Mathematics and Natural Sciences, University of Oslo. The work was carried out at the group of Electrochemistry under the supervision of Professor Truls Norby, Professor Reidar Haugsrud and Dr Tor Bjørheim during the period from August 2019 to June 2021.

I would like to thank my supervisors Truls, Reidar and Tor for their support throughout my M.Sc. work. I never would been able to complete my thesis had it not been for the dedicated and extremely helpful people at the group of electrochemistry. Special thanks to Masoud and Ragnar for teaching me about all the inner working of the electrochemistry (spaghetti) lab. Thanks to Sarmad for great discussions, teachings about space-charge theory and contributions to the thesis. Thanks to Xin for always asking if I need help with my DFT calculations, I almost always did, when passing me by in the corridors.

It might have been a miracle that I got my thesis ready on time in a year coloured by lockdowns draining all lifeforce and motivation. Had it not been for my great family and fantastic friends, it all would've been quite intolerable. Lastly, I would like to thank my dearest for unstoppable support and love, not to mention hours of proofreading. Together with you, a pandemic while writing a thesis actually weren't all that bad.

Oslo, June 2021
Erik Alsgaard

Summary

Proton ceramic fuel cells based on an yttrium-doped barium zirconate electrolyte might pose as a viable option for future hydrogen applications. High resistances in the electrolyte however hampers the performance of the material. Therefore, a novel heterostructure engineering strategy is applied in order to investigate alternative solutions to reducing the resistances. This thesis aims to deepen our understanding of how heterostructures and their interfaces might affect the electrolyte resistances. The goal of the following approach is to circumvent proton trapping at acceptor dopant sites. A job-sharing model has been investigated where one phase "supplies" the protons while the other phase conducts them. The proton donor phase is acceptor doped and more acidic than the other phase, resulting in a net transfer of protons over to the conductive phase. The latter phase, free of trap sites and enriched in charge carriers, is then hypothesized to exhibit a conductivity increase.

Modern computational methods allow for compositions to be investigated theoretically without having to perform tedious experiments. While experiments measure the actual effects of the system of interest, the results might be ambiguous as they often are a combination of several contributions. Theoretical computations on the other hand might give insight into trends, often on the atomistic scale, else impossible to separate from other effects experimentally. Combining the two methods, in depth knowledge and understanding of the system is acquirable.

The model system, an alternating multi layered $BaZr_{1-x}Y_xO_3/SrTi_{1-x}Sc_xO_3$ film was fabricated by pulsed laser deposition onto a (100) MgO substrate. The thin (60 nm) films were by X-ray diffraction confirmed to be grown epitaxially, made possible by a good lattice match between the substrate and the films. Impedance spectroscopy measurements of the $BaZrO_3/SrTi_{0.9}Sc_{0.1}O_3$ film showed a conductivity of 0.27 mS/cm, comparable to the conductivity of the reference $BaZr_{0.9}Y_{0.1}O_3$ film (0.28 mS/cm). The activation energy of the heterostructure was measured to 0.45 eV, lower than for the reference $BaZrO_3$ and $BaZr_{0.9}Y_{0.1}O_3$ films and in the range of the proton migration activation energy. The $SrTi_{0.9}Sc_{0.1}O_3$ had a larger activation energy of 0.64 eV, expected for oxide ion conduction mechanism.

When going to dry from humid atmosphere for the $BaZr_{1-x}Y_xO_3$ containing films was a decrease in conductivity of 55 % to 65 %, attributed to a decrease in charge carrier (proton) concentrations which was further confirmed by a hydrogen isotope exchange. A slope of 0.143 was observed in the Arrhenius plot of the $SrTi_{0.9}Sc_{0.1}O_3$ film, indicating that ionic defects dominate concentration-wise whilst minority holes contribute significantly to the conductivity in the measured pO_2 range.

First principles calculations of a $BaZr_{0.984}Y_{0.016}O_3H_{0.016}$ 4 by 4 supercell showed the energy difference a at set of $Y\text{-}H^+$ distances. The trapping energy of the protons was calculated as a function of in-plane strain and was found to increase with more negative (compressive) strain. Additionally, strain in general decreases the long-range mobility of protons in the yttrium dopants because of an energy barrier, larger than or equal to the trapping energy. Removing -0.5 % of strain was found to result in an activation energy decrease, increasing the conductivity by a factor of two. The calculated trapping energy change for different levels of strain agree well with experimental activation energies from literature [1].

Comparisons of measurements between reference films and the $BaZrO_3/SrTi_{0.9}Sc_{0.1}O_3$ heterostructure supports the job-sharing model. By assuming that the space charge region of the $BaZrO_3$ and $SrTi_{0.9}Sc_{0.1}O_3$ does not affect the conductivity of the latter, a conductivity increase of a factor of 14 was calculated for the $BaZrO_3$ layer of the heterostructure compared to the reference $BaZrO_3$ film.

List of abbreviations

gb – Grain boundary

sc – Space charge

tf – thin film

AC – Alternating current

DC – Direct current

IS – Impedance spectroscopy

PLD – Pulsed laser deposition

LDA – Localized density approximation

GGA – Generalized gradient approximation

SEM – Scanning electron microscopy

XRD – X-ray diffraction

DFT – Density functional theory

PBE – Perdew-Burke-Ernzerhof functional

PBEsol – Perdew-Burke-Ernzerhof functional revised for solids

VASP – Vienna ab-initio simulation package

BZO – Barium zirconate

BZY – 10 % yttrium doped BZO

BZYx – x % yttrium doped BZO

STO – Strontium titanate

STS – 10 % scandium doped STO

STSx – x % scandium doped STO

HArmix – 5 % H_2 and 95 % Ar gas mix

PCFC – Proton ceramic fuel cell

SOFC – Solid oxide fuel cell

KV – Kröger-Vink

Contents

Preface IV
Summary VI
List of abbreviations VIII
Contents X
1 Introduction 1
1.1 Motivation 1
1.2 Yttrium-doped barium zirconate 2
1.3 Approach 3
2 Theory 5
2.1 The perovskite structure 5
2.2 Defect chemistry 6
Kröger-Vink notation 6
Defect equilibria 7
Atmosphere dependency of defect concentrations 7
2.3 Transport 10
Diffusion 10
Electric conductivity 14
2.4 AC characterization 16
Impedance 16
Circuit elements 17
Deconvolution 18
2.5 Heterointerface engineering 19
Thin film heterostructure 19
Job sharing 21
Space charge 21
Strain 23
2.6 Quantum mechanical modelling 23
Density functional theory 24
Exchange and correlation approximations 25
3 Literature 28
3.1 Proton conducting perovskites 28

Proton trapping....29
Thin film barium zirconate....31
3.2 Heterostructure engineering....32
Deposition and structure....32
Space charge....33
Strain....34
Layered films....35
4 Experimental....38
4.1 Sample preparation....38
PLD....38
Electrode preparation....39
4.2 AC measurements....39
Apparatus....39
Conductivity measurements....41
4.3 Characterization....43
XRD....43
SEM....43
4.4 Modelling....43
Cells....44
Association energies....45
Hydration enthalpy....45
4.5 Errors....46
5 Results....48
5.1 Characterization....48
5.2 Impedance measurements....50
Constant temperature conductivity comparisons....50
Optimalization of film deposition....51
Temperature dependency....52
Atmosphere dependency....54
Other measurements....56
5.3 Computational....57
Static and dynamic cell volume....57
Relative proton-yttrium distances....58

Hydration energies 59
6 Discussion 61
6.1 Heterostructure 61
Optimalization 61
Heterostructure effect 63
The space charge effect on the heterostructure 66
Dehydration at high temperatures 67
6.2 Lattice strain 68
6.3 Further work 69
7 Conclusion 71
Appendix 78

1 Introduction

1.1 Motivation

The sudden increase in greenhouse gases the last 250 years is believed to be part of the reason for the present-day global temperature increase [2]. A shift from fossil to less polluting energy sources is therefore necessary in order to minimize climate change. Many governments are and have been subsidizing low carbon energy sources such as windmills and photovoltaic cells, accelerating the renewable energy market growth in the coming years [3]. The increase in renewable electric energy requires better electric grids or effective means of energy storage. Furthermore, as more modes of transportation are transitioning from fossil fuels to electricity, batteries are falling in short for long-distance travel, heavy transportation and aviation in terms of weight and charging time.

Hydrogen technology offers an alternative solution to all these problems. As a carbon-free energy carrier, hydrogen gas releases “zero” emissions on site having great potential for improving the air quality in large cities pestered by combustion engines pollutions. Hydrogen fuel cell operation is highly efficient while the electrolysis of H_2O to H_2 and O_2 is even more so. Compressed hydrogen gas offers high energy density, fuelling rate and can employ already exciting fossil fuel logistics infrastructure. Because of the ever-falling prices of Li-ion batteries and energy from natural gas which is has a lower carbon footprint compared to oil and coal however, hydrogen technology has yet to become competitive.

A typical fuel or electrolyser cell consist of three main components an oxygen and hydrogen electrode and an electrolyte separating the two electrodes. There are several kinds of fuel cells such as solid oxide fuel cells (SOFC) and polymer electrolyte membranes though; this thesis only deals with protonic ceramic fuel cells (PCFC). Fuel cells in general operate with high-energy efficiency and are therefore attractive for converting chemical energy to electricity [4]. PCFCs are usually operated at low to intermediate temperatures, in contrast to SOFCs which operate at high temperatures which often lead to mechanical and chemical stability issues. Furthermore because of the charge carriers being protons, the hydrogen is not diluted by water vapor. Much of the energy loss of the cell can be accounted to ohmic resistances in the electrolyte [5] and improvements must be made to minimize these losses in order to increase its energy efficiency. Such improvements being decreasing the electrolyte

thickness, increasing proton concentrations and finding materials with a higher proton mobility. Furthermore, factors such as stability and the need of lower operating temperatures to increase feasibility, need to be taken into account. One material which has shown great promise is barium zirconate however, much is left in terms of understanding the proton conduction mechanisms [6] needed to further improve the materials properties to its full potential.

1.2 Yttrium-doped barium zirconate

The materials class of perovskite type structures have for many years been investigated as possible PCFC electrolyte materials. One of those are the barium – transition metal oxides, barium cerate ($BaCeO_3$) being one of the first promising compositions [7-9]. However, under practical conditions the $BaCeO_3$ was shown to be prone to degradation when exposed to CO_2 at high temperatures forming carbonates [9]. A more stable alternative, barium zirconate ($BaZrO_3$), received much interest as it doesn't experience dehydration before reaching higher temperatures around 450 ℃ in humid atmosphere, has an appreciable bulk proton mobility and can withstand both reducing and oxidizing conditions in addition to carbon containing atmospheres [5].

$BaZrO_3$ belongs to a class of proton materials of which the nominal composition does not contain protons. Effective negative dopants are substituted into the lattice which in turn are charge compensated by effective positive defects such as protons. Yttrium dopants have been shown to yield good hydration and proton conductivity however, under the same ideal conditions $BaZrO_3$ exhibited lower conductivity than the $BaCeO_3$. Owing to high grain boundary resistance and decreased mobility from proton trapping sites [10]. Reducing the grain boundary density has been successful e.g. by growth of a grain boundary free single crystal [11]. Proton trapping occurs in the presence of the Y-dopants by strongly increasing the proton affinity of the closest oxide ions to the Y-dopant [12]. A recent publication from 2021 show an attempt of circumventing the trapping effect by two dimensional doping of $BaZrO_3$ [13]. A layered structure where every second layer is doped with yttrium was fabricated which applies a job-sharing effect where the undoped layer mainly conducts the protons while the other "supplies" them.

1.3 Approach

Heterostructure engineering opens up for new possibilities in materials science, as the materials properties are greatly affected by the microstructure. To fully make use of the possibilities heterostructure engineering poses, greater understanding of atomistic transport mechanisms especially by computationally heavy atomistic modelling, is necessary. Space-charge regions are an important part of heterostructures might govern the transport properties of the structures. While space charge regions are usually associated with proton depletion around grain boundaries in $BaZrO_3$, a space charge layer might also enhance the concentration of mentioned charge carrier depending on its potential. By better understanding the atomistic effects one may better tailor interfaces, microstructures and materials doping to one's advantage.

The starting point of this thesis is the computational study of Saeed et al.; *charge-carrier enrichment at $BaZrO_3$/$SrTiO_3$ interfaces* [14]. The calculations show that in the interface region $SrTiO_3$ acts as a proton donor and $BaZrO_3$ as a proton acceptor. The net transport of charge carriers from one material to the other is driven by a difference in defect formation energies, potentially increasing the proton conductivity. This thesis seeks to experimentally investigate the $BaZrO_3$/$SrTiO_3$ interface and to deepen the understanding its defect and transport mechanisms.

Another factor coming into play at interfaces is strain. When two different structures are conjoined, they adapt to the other resulting in a structural change. The structural changes further result in changes in the local potentials and bond strengths which affect the conductive properties. For interfaces between two materials of similar structure and with a good lattice match, one material might be grown epitaxially onto the other. By the materials choice and varying the thicknesses of the materials, the level of strain can be controlled. It can be difficult to isolate the effects from strain from e.g., space charge effects. Therefore, first principles atomistic modelling is used to calculate the effect of strain on the proton mobility in $BaZrO_3$.

Heterostructure layered films have been fabricated by a pulsed laser deposition method. The defect chemistry of the films is investigated using impedance spectroscopy, while structural characterization was performed using x-ray diffraction and scanning electron microscopy.

2 Theory

2.1 The perovskite structure

The perovskite structure (ABO_3) consists of corner sharing BO_6 octahedra with large *A* cations in the cavities coordinated to twelve oxide ions (Figure 1). The perovskite has become a popular material class among materials scientists because of its ability to take a large range of different constituent ions. The ions might have a large range of ionic radii, electronegativity and oxidation states. The flexibility of the structure allows for large dopant concentrations. By tuning the composition of the perovskite many functional properties including ionic conductivity can emerge.

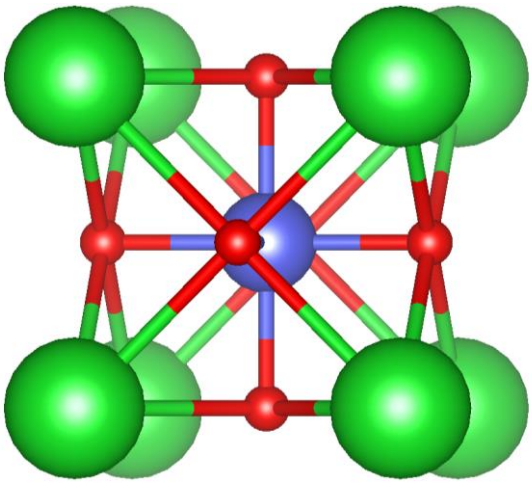

Figure 1. The cubic perovskite structure, green and blue bulbs signify the *A* and *B* cation respectively and the red the *O*. Image drawn using Vesta (JP-Minerals).

The corner sharing octahedra are able to contract or expand along an axis in order to facilitate for non-ideal sized constituents. The Goldschmidt tolerance factor *t* (1) gives the crystal system given the ionic radii r_i. For both $SrTiO_3$ (STO) and $BaZrO_3$ (BZO) the equation correctly predicts a cubic crystal system, $0.9 < t < 1.0$. For perovskites with *t* outside this range crystal systems with lower symmetry e.g., tetragonal symmetry is adopted.

$$t = \frac{r_A + r_O}{\sqrt{2}(r_B + r_O)} \tag{1}$$

2.2 Defect chemistry

Defects that are limited to one lattice site are called *point defects* and are zero-dimensional. Though, at high concentrations, point defects might stabilize thermodynamically by forming 1-dimensional dislocations or 2-dimensional plane defects such as grain boundaries. Such defect structures might also be a result of e.g., lattice strain, sintering of differently oriented grains and interfaces between different phases.

Defect chemistry assumes a fully ionic bonding approach, this is not true for all oxides and most of their bonds are to a varying degree of covalent or ionic. However, a fully ionic model has proven to describe defects situations with good accuracy for low defect concentrations. At higher defect concentrations, the model becomes inaccurate because of defect association as the electrostatic forces between the charged defects begin to strongly interact.

Dopants are ions, usually cations, added to the material with effective negative or positive charge and are called acceptors or donors, respectively. In wide bandgap oxides such as BZO, effectively charged dopants are often added in order to increase the concentration of more mobile ionic charge carriers, typically protons or oxygen vacancies.

Kröger-Vink notation

In order to write these defects and their reactions efficiently, the Kröger –Vink (KV) notation is commonly adopted. The notation consists of three elements: A_B^C where *A* denotes the species, *B* the lattice site and C the effective charge of the defect. A represent defects by their atomic symbol and vacancies by a "*v".* The lattice site (*B*) is either a regular lattice site or an interstitial one written "*i*". Lastly is the upper-case symbol of the KV notation, *C*. An ion's formal oxidation number dictates the effective charge of the defect, but one must keep in mind that they might adopt several other oxidation states. To demonstrate; an yttrium ion substituted on a zirconium site with oxidation number +3 and +4 respectively, results in an effective charge of -1 written in KV notation as $Y_{Zr}^{/}$. Where "/" denotes one negative effective charge, the other effective charge symbols are "*x" for* neutral and "•*"* for positive effective charge. A special case are interstitial protons, written $H_i^{\bullet}$. Because of their small size and large charge density they do not occupy normal lattice sites but are instead localized in the electron cloud around oxide ions (Figure 5) (or other anions such as nitrogen defects) [15, 16]. Therefore, $OH_O^{\bullet}$ is a more accurate way to describe the defect.

Defect equilibria

Ionic defects are mobile at high temperatures and given enough time they may move around and approach thermodynamic equilibrium. Though, cooled to sufficiently low temperatures the defects become relatively immobile and dubbed “frozen in”. The defects unable to move, will not be able to reach equilibrium if not already there.

The equilibrium constant *K* for a chemical reaction (2), may be related to the standard Gibbs free energy change through equation (3). A, B and C are reactants and the product, and the upper-case letter variables are integers. The activities *a* are given as the actual concentrations at equilibrium divided by their respective standard state concentrations. Therefore, the Gibbs energy change is expressed as the Gibbs standard energy change ΔG^0.

$$xA + yB = zC \tag{2}$$

$$K = \left(\frac{[reactants]}{[products]}\right)_{eq} = \left(\frac{a_C^z}{a_A^x \cdot a_B^y}\right)_{eq} = \exp\frac{\Delta S^0}{R} \cdot exp\frac{-\Delta H^0}{RT} = exp\frac{-\Delta G^0}{RT} \tag{3}$$

The expression can also be applied to solids, by thinking of the defects as a dilute non-interacting solute and the material as a solvent.

Atmosphere dependency of defect concentrations

Ionic, electron and hole conductivity in acceptor-doped barium zirconate and strontium titanate are highly affected by atmospheric changes. Acceptor dopants are typically charge compensated by either holes, oxygen vacancies or protons. Their ratio can often be tweaked by adjusting the gas pressure. The charge neutrality must be upheld according to

$$\sum_i ez_i c_i = 0 \tag{4}$$

where ez_i is the effective charge, and c_i the concentration of defect *i*.

A humid atmosphere increases the proton concentration through equation (5). Without going into detail on the mechanics, a proton goes to an oxide ion site while the remaining hydroxide occupies a vacant oxide ion site.

$$H_2O\ (g) + \ O_o^x + v_o^{\bullet\bullet} = 2OH_O^{\bullet} \tag{5}$$

Protons dominate concentration wise in BZO under humid conditions at low and up to intermediate temperatures and are not as greatly affected by the partial oxygen pressure pO_2. However generally, under oxidizing conditions oxygen vacancies will be consumed if present, resulting in holes:

$$\frac{1}{2}O_2(g) + v_o^{\bullet\bullet} = O_o^x + 2h^{\bullet} \tag{6}$$

Under highly oxidizing conditions cation vacancies might form, charge compensated by holes.

$$\frac{3}{2}O_2(g) = 3O_o^x + 6h^{\bullet} + v_{Ba}^{//} + v_{Zr}^{////} \tag{7}$$

Though holes are most common in acceptor doped oxides, electrons might also occur in very reducing atmospheres:

$$H_2(g) + O_o^x = H_2O\ (g) + \ v_o^{\bullet\bullet} + 2e^{/} \tag{8}$$

The latter defect reaction has water vapor and oxygen vacancies at the right-hand side, combining it with (5) it becomes obvious that reducing the sample can increase both proton and electron concentrations. However, this is undesirable for electrolyte performance as electron defects give parasitic contributions, reducing the performance of e.g., a fuel cell.

Under any atmosphere the system must follow the electroneutrality condition (4). Here the acceptor dopant *Acc* is substituted on the B site of the perovskite giving the total electroneutrality condition for the involved defects:

$$[h^{\bullet}] + [v_o^{\bullet\bullet}] + [OH_O^{\bullet}] = \left[e^{/}\right] + \left[Acc_B^{/}\right] + 3\left[v_M^{///}\right] \tag{9}$$

A Brower diagram shows the calculated defect concentrations as a function of partial pressures. When calculating the Brouwer diagrams (Figure 2) the zirconium and barium vacancy concentrations are assumed to be equal, thus expression (7) is simplified by substitution of the following equation:

$$v_{Ba}^{//} + v_{Zr}^{////} = 2v_M^{///} \tag{10}$$

(a)

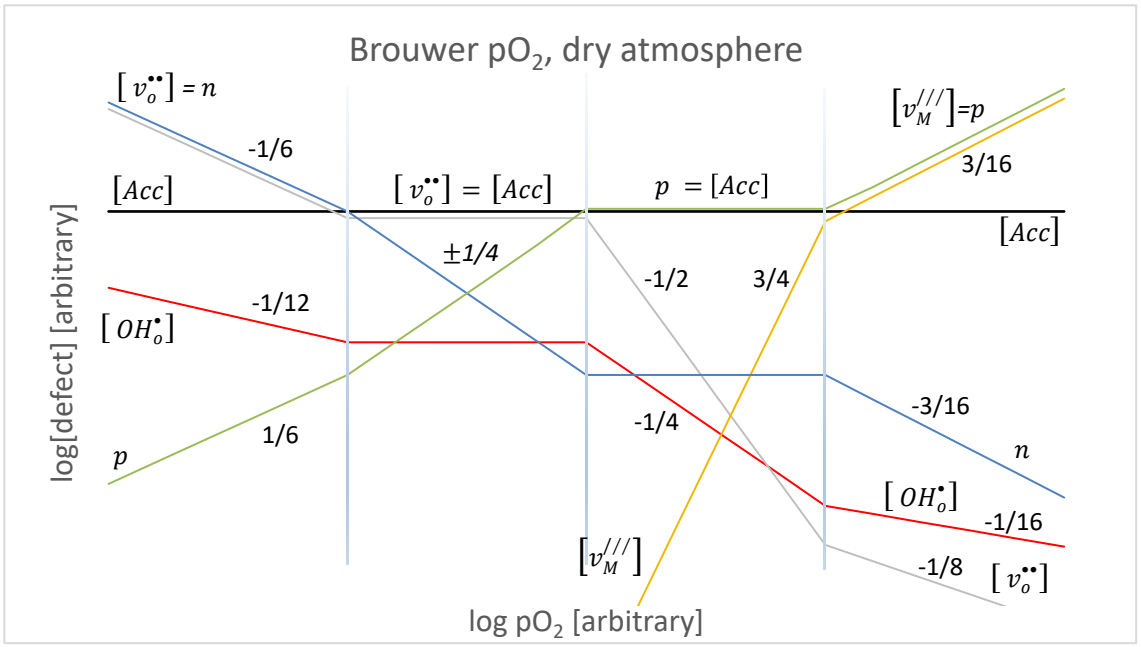

(b)

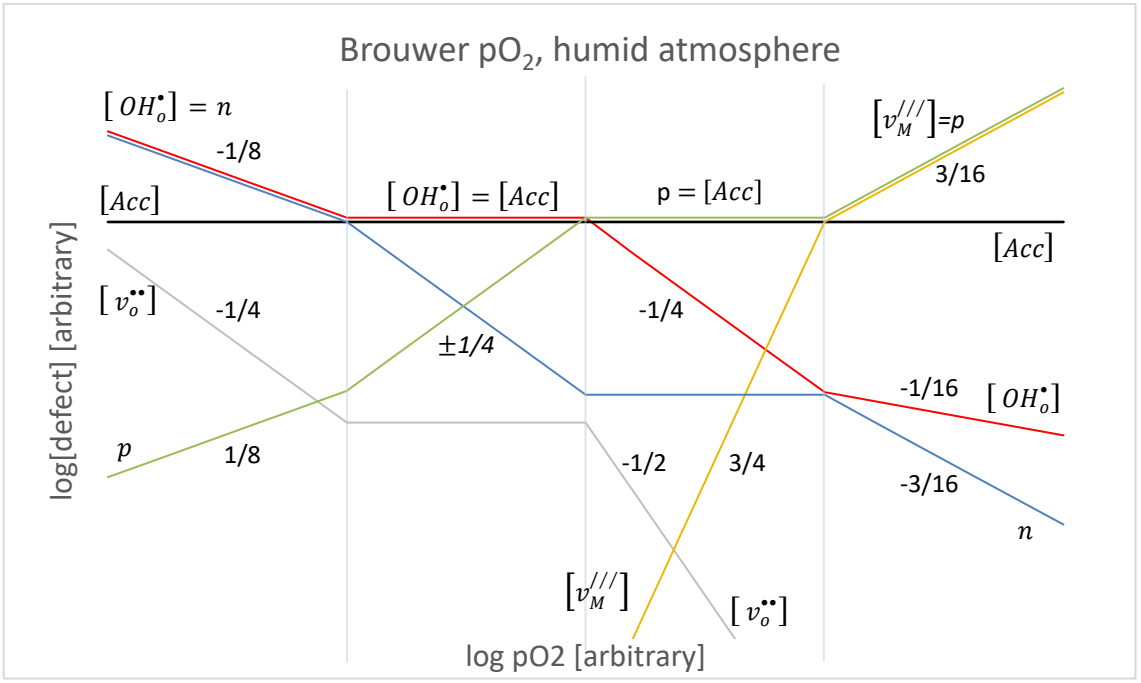

Figure 2. Brower diagrams representing the defect concentrations in acceptor doped perovskites. The defect concentrations are given for BZY equilibrated in humid (a) and dry (b) atmosphere.

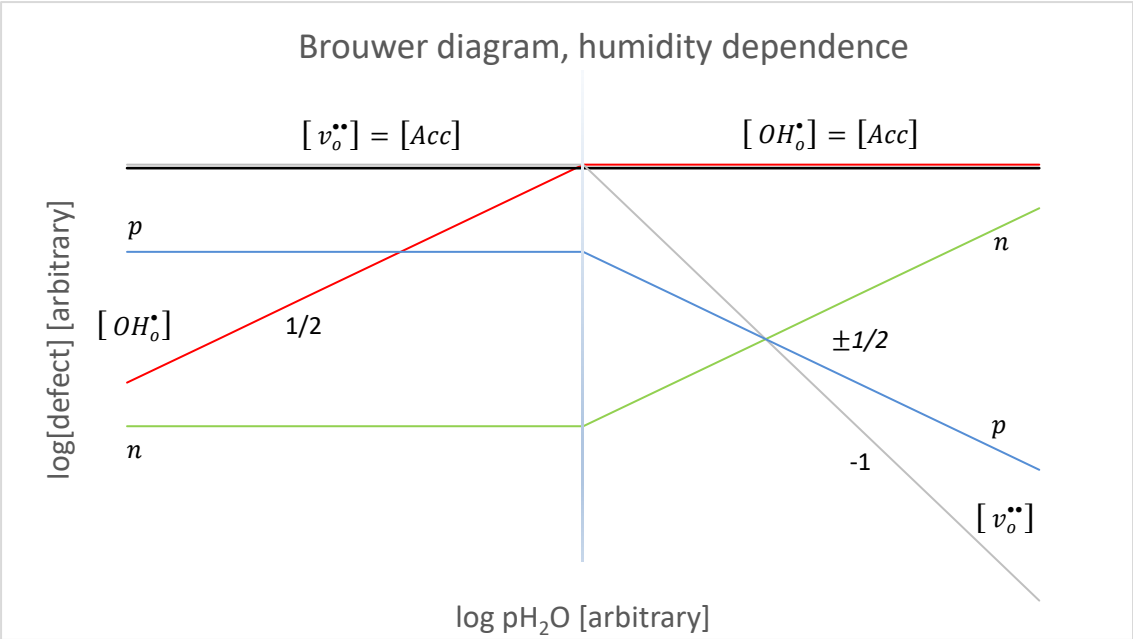

Figure 3. Brouwer diagram showing defect concentration dependencies of the water vapor pressure.

One may calculate the Brouwer diagram by first knowing the possible defect species in a material, Y-doped BZO in this case. Thereafter by finding defect reactions relating them to each other, their dependencies of each other can be found. Relating the equilibrium constant expressions (3) of the defect reactions (5) (6) (8) (7) and adding electroneutrality (9) as a constraint, it is possible to derive the defect concentrations as function of activity. Furthermore, by assuming a set of dominating defects at an activity range, the problem might be solved for complex systems of many possible defects. The dominating defects, ideally two of opposite charge, create a simplified electroneutrality condition where all minor defects are omitted. The atmosphere dependencies are illustrated for Y-doped BZO (BZY) in a Brouwer diagram (Figure 2).

2.3 Transport

Diffusion

The flow of particles in a concentration gradient is described by Fick´s first law:

$$j_i = -D_i \frac{dc_i}{dx} \tag{11}$$

Where *j* is the flux (particles crossing a cross-section area per unit time), D_i the random diffusion coefficient, *c* the concentration and *I* the defect species. So, following the equation the particles will move from high to low concentrations (hence the negative right-hand side).

The Nernst-Einstein relation (12) relates the diffusion coefficient to the mechanical mobility B, the temperature and Boltzmann's constant k_B.

$$k_B T B_i = D_i \tag{12}$$

Defects can move in between sites but must overcome an energy barrier of migration ΔH_m in order to migrate to another site. The random diffusion coefficient may in addition to the term above be expressed in terms of ω, the frequency of jumps of energies higher than or equal to the ΔH_m.

$$D_i = \alpha a_0^2 \omega N_d \tag{13}$$

The equation (13) includes a geometric factor α, the lattice constant a_0^2 and the defect concentration N_d.

The defect concentrations may be described by the enthalpy and entropy of defect formation, ΔH_d and ΔS_d:

$$N_d = e^{\Delta S_d / k_B} \cdot e^{-\Delta H_d / k_B T} \tag{14}$$

Similarly, one may express the jump frequency ω in terms of the enthalpy and entropy of migration, ΔH_m and ΔS_m, and a vibrational frequency ν as shown in equation (15).

$$\omega = \nu \cdot e^{\Delta S_m / k_B} \cdot e^{\Delta H_m / k_B T} \tag{15}$$

Inserting equations (14) and (15) into (13) results in a modified diffusivity expression (16), depending on both the defect formation and migration enthalpies and entropies.

$$D = \alpha a_0^2 \nu e^{\frac{\Delta S_m + \Delta S_d}{k_B}} e^{-\frac{\Delta H_m + \Delta H_d}{k_B T}} = D_0 e^{-\frac{\Delta H_m + \Delta H_d}{k_B T}} \tag{16}$$

The vibrational frequency and entropies are for practical purposes defined as a preexponential factor D_0 (17).

$$D_0 = \alpha a_0^2 \nu e^{\frac{\Delta S_m + \Delta S_d}{k_B}} \tag{17}$$

Generally, the activation energy is defined as $E_a = \Delta H_m + \Delta H_d$. However, under conditions where the defects are assumed to be frozen in, $N_d = N_{d,frozen}$ is constant, can equation (16) be simplified

$$D = \alpha a_0^2 \nu N_{d,frozen}\, e^{\frac{\Delta S_m}{k_B}}\, e^{-\frac{\Delta H_m}{k_B T}} \tag{18}$$

and the activation energy is approximated as $E_a \approx \Delta H_m$.

Four ionic diffusion mechanism will be described in this second half of the section, focusing on oxide ion and proton diffusion. Ions in materials can be illustrated as spheres, where the larger ones constitute the packing spheres and smaller ones reside in the empty volume in between. Tightly packed, large ions will typically not be able to move in between the other ions but will need a vacancy in order to migrate. This mechanism is named the vacancy mechanism, and the conductivity related to this mechanism is dependent on the concentration of vacancies of the mobile ion. Small ions don't always need vacant neighbouring positions to move. They are able to occupy interstitial sites and may move between them.

Protons are small and may easily move in between lattice ions, jumping from interstitial-to-interstitial position in an interstitial mechanism. The Grotthuss mechanism [17] is named after one of the pioneers of electrochemistry (and photochemistry) Theodor von Grotthuss. The mechanism divides the migration of protons into two steps. First the reorientation of the hydroxide dipole moment where the proton rotates around the oxide ion, and second the proton jumps to a neighbouring oxide ion. The rotation requires little energy compared to the jump and the latter is the limiting factor. A short series of such jumps and rotations is illustrated in (Figure 4).

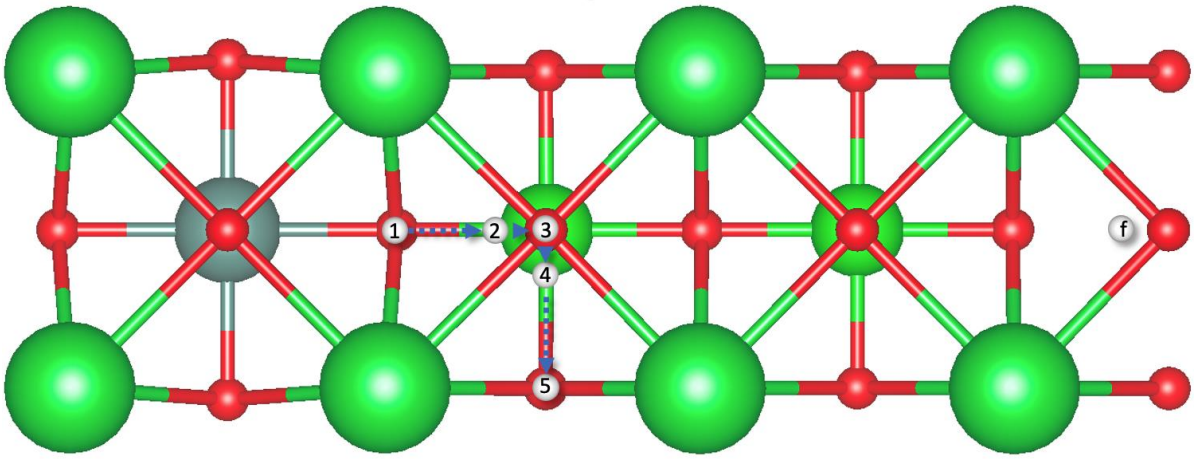

Figure 4. A proton transport pathway of a single proton. The arrows between 1-2 and 4-5 signify proton jumps between oxide ions, while the 2-3 and 3-4 are 90 ° rotations around a single oxide ion. The 1, 2, 3, 5 and f labelled protons are later referred to with respect to the yttrium-proton distance as 1NN (1st Nearest Neighbour), 2NN, R2NN (Rotated), 3NN and "far" respectively. The white circle signifies a proton, red – O, small green – Zr, large green – Ba, grey - Y. The image is drawn using Vesta (JP-Minerals).

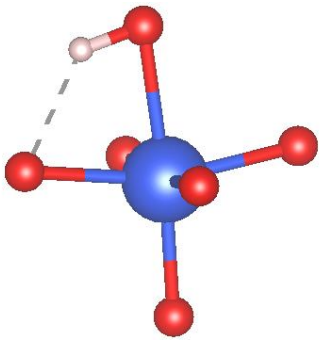

Figure 5. A ZrO_6 octahedra of $BaZrO_3$ showing a proton (white) bonded closely to an oxide ion. The OH-Zr-O angle is reduced to 77 ° compared to 90 ° of an ideal cubic perovskite because of the electrostatic attractive forces between the oxide ions and the proton (calculated using VASP). Image drawn using Vesta (JP-Minerals).

The vehicle mechanism occurs, quite pictorially, when an oxide ion with an associated proton jumps to a vacant oxide ion site. The hydroxide ion is smaller than an oxide ion and may therefore have a lower activation energy for the migration. However, the activation energy for a hydroxide ion jump is higher than for protons, making the Grotthuss mechanism the dominating mechanism for proton transport in most cases.

Defects introduce local variations in the lattice which might induce traps, detrimental to protons transport. The traps being sites which require a higher energy for the proton to jump from, compared to ordinary sites in a homogeneous defect free lattice. In BZY the trapping effect related to the Y-dopant is related both to chemical and structural aspects. The Y^{3+} is slightly larger than the Zr^{4+}, 0.9 Å and 0.72 Å respectively [18], distorting the surrounding lattice. A hydroxide neighbouring the Y results in a slight relaxation of the lattice as the

hydroxide is smaller than an oxide ion. Also, the effective negative Y-dopant increases the basicity of the adjacent oxide ions, efficiently increasing the proton affinity of the oxide ions.

Electric conductivity

Charged species will experience a force *F* in an electric potential ϕ which depends on the species charge and the electric field strength *E*

$$F_i = -z_i eE = -z_i e\frac{d\phi}{dx} \tag{19}$$

where *e* is the elemental charge and z_i the charge of species *i*.

The mobility of the defects *B* is a measure of the mechanical transferability of the defects from one site to another. Defined as the average drift velocity *v* of a defect *i* divided by the driving force F_i:

$$B = \frac{v_i}{F_i} \tag{20}$$

When measuring conductivities of materials, the charge mobility μ is of greater interest, defined as:

$$\mu_i = |z_i|eB \tag{21}$$

The conductivity σ_i of a material can be found from the current density i_i.

$$\sigma_i = \frac{i_i}{E} = |z_i|ec_i u_i \tag{22}$$

This is a helpful relation as it shows that the partial conductivity scales with charge, charge carrier concentration and charge mobility.

Expressing the conductivity in terms of the diffusivity can be done by using the Nernst-Einstein relation, by combination the two equations (12) and (22) resulting in equation (23).

$$\sigma_i = \frac{c_i \cdot (z_i e)^2}{k_B T} D_i \tag{23}$$

Substituting the diffusivity of equation (16) into equation (23) gives the following equation for the conductivity of species *i*:

$$\sigma_i = \frac{\sigma_{0,i}}{T} e^{-\frac{\Delta H_{i,m} + \Delta H_{i,d}}{k_B T}} \tag{24}$$

The preexponential factor $\sigma_{0,i}$ is defined as:

$$\sigma_{0,i} = \frac{c_i \cdot (z_i e)^2}{k_B} D_0 \tag{25}$$

At high temperatures most materials show some n- or p-type conductivity, as is the case for semiconductors even at low temperatures. In polar oxides the conduction mechanisms differ between large and small polarons, whereas small polarons usually are better suited for describing transition metal oxides, such as BZO. A polaron is the combination of an electron or hole and its associated distortion, and they distort the surrounding lattice in polar materials because of electrostatic interactions. In the low temperature range below 500 °C, the polarons move by a tunnelling mechanism between localized sites. The electronic charge mobility is determined by lattice scattering and therefore the conductivity decreases with increasing temperature following the relation:

$$u_e = u_{e,0} T^{-3/2} \tag{26}$$

Where the u_e is the charge mobility of the electronic species, holes or electrons, and $u_{e,0}$ its temperature independent part. At higher temperatures >500 ºC the mobility of electrons and holes can no longer be described by the band theory. Instead, they can be seen as trapped species which may hop between sites with an activation energy E_u. The Nernst-Einstein relation can be used to relate the mobility to the temperature through the following equation.

$$u_e = \frac{e}{k_B T} D = \frac{u_0}{T} exp\left(\frac{-E_u}{k_B T}\right) \tag{27}$$

For mixed conductors having several mobile charged species it is helpful to know the ratios between different charge carriers. The transport number t_i describes this ratio, given as the partial conductivity σ_i of a species *i* divided by the total conductivity σ_{tot} as shown in equation (28).

$$t_i = \frac{\sigma_i}{\sigma_{tot}} \tag{28}$$

For barium zirconate at lower temperatures its proton concentration and conductivity are much higher than the hole and oxygen vacancy conductivity. Therefore, for simplicity one may use the approximation $t_{proton} \approx 1$ without introducing large errors.

2.4 AC characterization

By applying an alternating current to a sample, it is possible to separate different conduction mechanisms. Fast transport mechanisms that usually don't exhibit any capacitive behaviour under a constant current might exhibit a measurable capacitance at high frequencies. Slower processes will similarly have a capacitive contribution at lower frequencies.

Impedance

Impedance measurements are commonly adopted to understand the electrochemical properties of conductive materials. It is an important tool because it allows one to separate different contributions to the impedance. A sinusoidal voltage *U* can be expressed as

$$U = U_0 \cdot \sin(\omega t) \tag{29}$$

where U_0 is the voltage amplitude and ωt the phase angle. The current response in a conductive material is then given by:

$$I = I_0 \cdot \sin(\omega t + \varphi) \tag{30}$$

Where φ is the out of phase component of the current response and I_0 the current amplitude. If $\varphi = 0$ then the current response is instantaneous and in phase or if $\varphi = \pi/2$ the current response is fully lagging behind the voltage. The impedance is defined as:

$$Z = \frac{|U|}{|I|} \tag{31}$$

Dividing the impedance into a real in phase component and an imaginary out of phase component it can be written in cartesian form as following:

$$Z = Z' + jZ'' \tag{32}$$

Where $Z´$ is commonly called the resistive component and $Z´´$ the reactive component of the impedance. The opposite of the impedance is the admittance Y, which is also a complex number consisting of the real conductance $Y´$ and the imaginary susceptance $Y´´$.

$$Y = Y´ + jY´´ \tag{33}$$

Impedance measurements are typically visualized in a Nyquist plot where the x-axis is the real part of the impedance, and the y-axis is the negative of the imaginary part (Figure 6). The measurement is performed by measuring from high to low frequencies in a so-called impedance sweep. The Nyquist plot ideally has a semicircle for each important polarization resistance along the real axis. A high frequency semicircle is typically dedicated to the bulk transport impedance, middle frequency the grain boundary and low frequency the electrode interface. The width of each semicircle can thereafter be assumed to be equal to the ohmic resistance of each contribution.

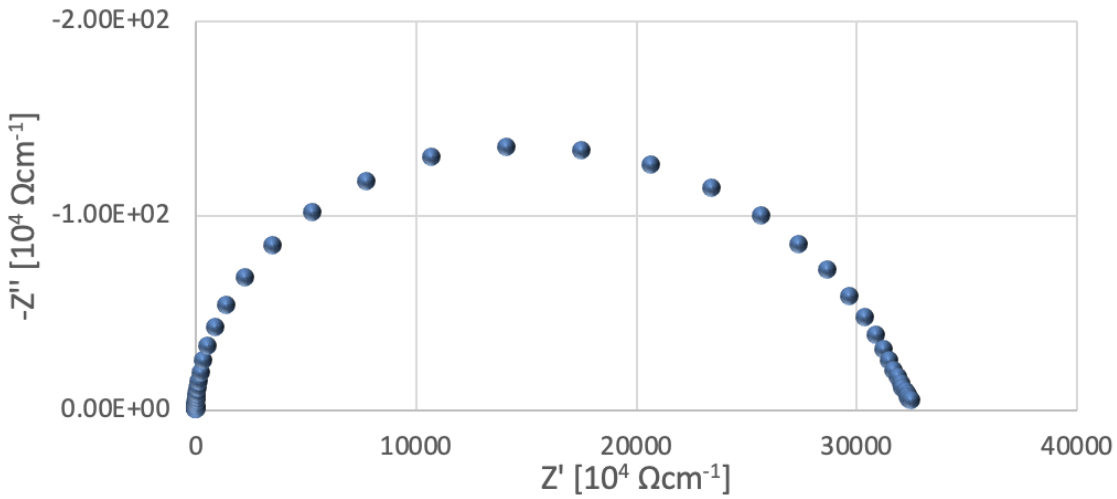

Figure 6. Nyquist plot of showing a typical impedance spectrum from high to low frequencies corresponding to chart points from the left to the right respectively.

Circuit elements

To analyse the impedance plots, circuit models are created and fitted to the experimental data. This is done by connecting individual circuit element in either parallel or series.

The resistor only includes the real part of the impedance, it is in other words an element with an instant current response where charge carriers only experience an ohmic resistance.

A capacitor does not conduct charge as a resistor does, but it can store a limited amount of electrostatic charge. Because it is insulating it only has a reactive contribution to the impedance given by the capacitance *C* and angular frequency ω:

$$Z_C = -j\frac{1}{\omega C} \tag{34}$$

Sometimes the two above elements are inadequate for fitting the impedance spectra. This is the case when the semicircles are depressed, which is typical for solids consisting of grains and grain boundaries. The depressed semicircle can often be seen as two or more intergrown semicircles. A constant phase element (CPE) solves this problem by acting as a hybrid of the resistor and capacitor. The impedance of a CPE is expressed as:

$$Z_{CPE} = Z'_{CPE} + Z''_{CPE} = Z_0\omega^{-n}cos\left(\frac{n\pi}{2}\right) - jZ_0\omega^{-n}sin\left(\frac{n\pi}{2}\right) \tag{35}$$

Where n =1 for a pure capacitor and n = 0 for a pure resistor. Z_0 is a frequency independent constant.

Deconvolution

To understand an impedance sweep and to quantify the different polarization resistances of a sample it is often necessary to deconvolute the spectra. It means to combine the different circuit elements and their mathematical expressions to represent the real system in the best possible manner. The elements may be added either in series or in parallel. Series addition is quite simple as the two impedances Z_1 and Z_2 sum up to the total impedance:

$$Z_{series} = Z_1 + Z_2 \tag{36}$$

However, for parallel elements the impedances cannot be added by simple summation, rather they follow the two formulas below, divided into the resistive and reactive parts for simplicity:

$$Z'_{Parallel} = \frac{Z'_1Z'_2\left(Z'_1 + Z'_2\right) + Z'_1Z''^2_2 + Z'_2Z''^2_1}{\left(Z'_1 + Z'_2\right)^2 + \left(Z''_1 + Z''_2\right)^2} \tag{37}$$

$$Z''_{Parallel} = \frac{Z''_1 Z''_2 \left(Z''_1 + Z''_2\right) + Z''_1 {Z'_2}^2 + Z''_2 {Z'_1}^2}{\left(Z'_1 + Z'_2\right)^2 + \left(Z''_1 + Z''_2\right)^2} \quad (38)$$

Inserting the two above formulas into equation (32) will give the parallel impedance. The circuit showed in (Figure 7) is a simple one but none the less able to accurately fit to most of the electrochemical IS data. The impedance of the circuit follows from the three derivations above and using the circuit elements as depicted (Figure 7) gives:

$$Z'_{circuit} = R_1 + \frac{R_2 \cdot Z'_{CPE,1}\left(R_2 + Z'_{CPE,1}\right) + R_2 \cdot {Z''_{CPE,1}}^2}{(R_2 + Z'_{CPE,1})^2 + {Z''_{CPE,1}}^2} \quad (39)$$

$$Z''_{circuit} = \frac{R_2^2 \cdot Z''_{CPE,1}}{(R_2 + Z'_{CPE,1})^2 + {Z''_{CPE,1}}^2} \quad (40)$$

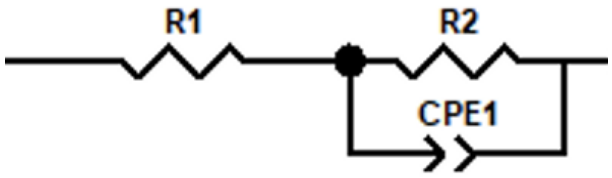

Figure 7. The circuit used to model the impedance sweeps, consisting of a resistance in series with a parallel resistance and CPE element.

2.5 Heterointerface engineering

Thin film heterostructure

Nanostructures often exhibit vastly different properties compared to the bulk materials, the interface induces strain and alters the fermi level resulting in electron transfer and a space charge region.

For studying interface effects, a multi-layered structure is easy to manufacture and allows for great tunability. The thin structure and high interface area versus volume allows for the interface effects to be measurable, which otherwise would be impossible.

The interface of two materials is best studied in a heterostructure, in this case an alternating layered heterostructure consisting of two chemically different materials, but structurally similar. The latter is important in order to achieve epitaxial single crystalline layers.

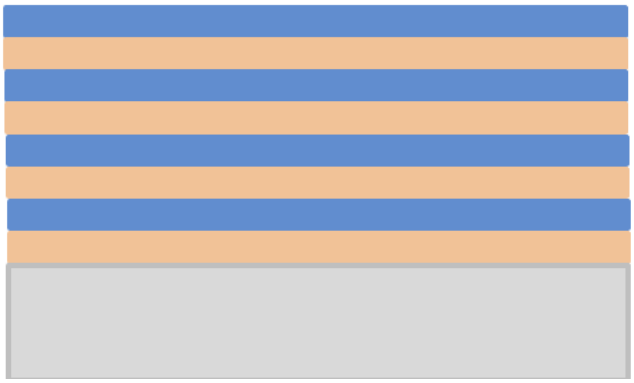

Figure 8. Diagram of a heterostructure thin film of two different phases (blue and orange) on a much thicker substrate (gray).

Thin film deposition allows for epitaxial growth, where new crystalline structure is formed in a well-defined orientation with respect to the substrate. Thus, allowing for preparation of single crystals. The different chemistry of two phases might induce a heterogeneous doping of the one or both of the phases. E.g., if one phase is rich in mobile species such as protons, the other phase might experience an enrichment of H^+ ions near the interphase region. The segregation energy is used to describe the willingness of a defect to move from one phase to the other

These effectively positively charged defects aren´t necessarily charge compensated locally resulting in a space charge region. The uncompensated heterogeneous doping reaction can be written in an unformal way ignoring the law of charge conservation of defect chemistry.

$$OH^{\bullet}_{O,doped} + O^{x}_{O,pure} = + O^{x}_{O,doped} + OH^{\bullet}_{O,pure} \quad (41)$$

The subscript denotes whether the structural site is located in an, in this case acceptor doped phase or a pure undoped phase. Here a proton moves across the interface from the doped phase to the undoped one, creating a negative and positive charge at each side of the interface respectively. Summing the charge over the interface region one can still see that the region as a whole remains charge neutral.

$$\sum_i n_i e z_i = 0 \tag{42}$$

The variable n_i is the number of defects i in the interface region.

Job sharing

Materials where different parts or phases have different roles are typically termed to be utilizing a job-sharing effect. Typically job sharing is associated with defect storage [19], but here the concentration increase is utilized for bettering the conductivity. Y-doped $BaZrO_3$ suffers from the trapping effect around the acceptor dopants. Heterogeneously doping the $BaZrO_3$ results in no yttrium dopants being present in the phase, circumventing the trapping effect. On the other side acceptor doped $SrTiO_3$ (STO) can donate some of its protons to the $BaZrO_3$. In principle such a job-sharing compound could achieve higher conductivities compared to the state-of-the-art Y-doped $BaZrO_3$ electrolyte.

Space charge

Space charge theory has proven a strong tool for predicting ionic conductivity in interface regions [20]. Interfaces and grain boundaries break the periodic bulk structure, such interruptions can be expected to be the origin of space charges. Such interruptions are typically grain boundaries and interfaces. Oxygen vacancies has a lower formation energy in the BZY grain boundary core, which in turn will lead to a net positive charge in the core. The net charge will increase the concentrations of oppositely charged defects and decrease concentrations of defects with the same charge in the vicinity of the grain boundary, the space charge region. Assuming a perfect cube on cube lattice match between BZO and STO there will be no grain boundary in between the two phases. However, the two materials have different defect formation energies, which in turn lead to a net transfer of defects from one phase to the other, creating a space charge. The strength of the space charge region, the Schottky barrier $\Delta\varphi(0)$, is measured as the potential difference between the boundary and the bulk.

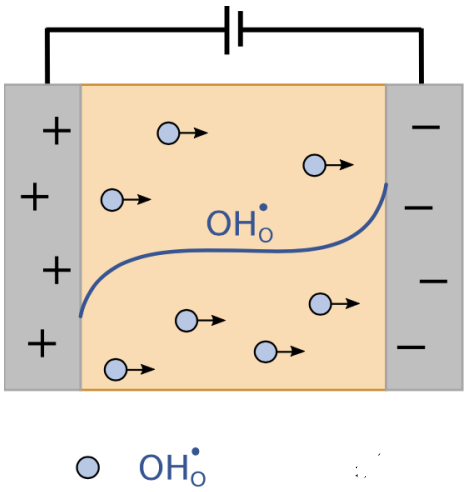

Figure 9. Diagram visualizing the proton concentration in a thin electrolyte (yellow) in contact with a negative and positive electrode interface (grey). A grain boundary will affect the protons similarly as the positive electrode, creating a negative space charge layer adjacent to the positive charge in order to create a net zero charge. Similarly, a negative charged layer can increase proton concentrations in its vicinity [21].

Defect concentrations by DFT

The space charge region may be calculated using atomistic modelling as shown by Polfus et al. [22]. The defect formation energies are calculated in the boundary core and in the bulk. In the bulk the electrochemical potential $\tilde{\mu}_{i,b}$ of defect i is simply given by the chemical potential. Because the bulk is the reference state, the bulk electrical potential is $\varphi_b = 0$.

$$\tilde{\mu}_{i,b} = \mu_{i,b} = \mu^{\circ}_{i,b} + k_B T \cdot \ln c_{i,b} \tag{43}$$

The core and space charge layer, abbreviated *c* and *sc* respectively, do not attain electroneutrality by themselves. The electrical potential is thus included in their electrochemical potential expressions:

$$\tilde{\mu}_{i,c} = \mu^{\circ}_{i,c} + k_B T \cdot \ln c_{i,c} + z_i e \varphi_c \tag{44}$$

$$\tilde{\mu}_{i,sc} = \mu^{\circ}_{i,sc} + k_B T \cdot \ln c_{i,sc} + z_i e \varphi(x) \tag{45}$$

$\varphi(x)$ is the electrical potential at a distance x from the core, and we define $\varphi(\infty) = \varphi_b$. By assuming low defect concentrations, the defect concentration is found to be equal to

$$c_{i,b} = N_b \, exp\left(\frac{E^f_{i,b}}{k_B T}\right) \tag{46}$$

where N_b is the total number of possible sites and $E_{i,b}^f$is the formation energy of defect *i* in the bulk. The electrochemical potential is assumed constant throughout the material and combining equations (43) and (44) the defect concentrations in the core is found to be:

$$c_{i,c} = \frac{N_c c_{i,b}}{N_b} exp\left(-\frac{E_{i,c}^f - E_{i,b}^f + z_i e\varphi_c}{k_B T}\right) \tag{47}$$

And combining (43) and (45) gives the defect concentration of the space charge layer:

$$c_{i,sc} = c_{i,b}\ exp\left(-\frac{z_i e\varphi(x)}{k_B T}\right) \tag{48}$$

Strain

Materials grown epitaxially must have a matching lattice constants and crystal structure, too large lattice constant deviations lead to dislocations. Barium zirconate deposited onto magnesium oxide will experience an in-plane strain described by the film-to-substrate mismatch *f*

$$f = \left(a_{0,substrate} - a_{0,film}\right)/a_{0,film} \tag{49}$$

where a_0 is the lattice constant of either the substrate or film assuming a perfect epitaxially grown film which usually is assumed for $f < 0.01$ at film thickness around 100 nm. A positive *f* would mean that the film is subjugated to a tensile strain while a negative value would mean the film is compressed biaxially. If a thick film is deposited the film will eventually relax itself by creating structural defects such as grain boundaries, reducing the effective strain on the film.

2.6 Quantum mechanical modelling

To describe macroscopic materials, one must take into account the numerous interactions and movements between nuclei and electrons, a highly complicated task. To understand how density functional theory attacks this problem one must first quickly review the many particle problem. Theory from this subchapter is taken from [23].

The nonrelativistic, time independent Schrödinger equation used to solve such systems is:

$$\hat{H}\psi_i = \hat{E}\psi_i \tag{50}$$

Where $\hat{H}$ is the Hamiltonian operator which works on the set of eigenstates ψ_i. For each eigenstate there is an associated eigenvalue E_i. The Hamiltonian operator is divided into several parts, firstly it has to take into account the movement and kinetic energy of the nuclei $T_N(\boldsymbol{R})$ and the electrons $T_e(\boldsymbol{r})$. Secondly are the potentials between the particles, nucleus-nucleus $V_{NN}(\boldsymbol{R})$, electron-nucleus $V_{Ne}(\boldsymbol{R},\boldsymbol{r})$ and electron-electron $V_{ee}(\boldsymbol{r})$ interactions.

$$\hat{H} = T_N(\boldsymbol{R}) + T_e(\boldsymbol{r}) + V_{NN}(\boldsymbol{R}) + V_{Ne}(\boldsymbol{R},\boldsymbol{r}) + V_{ee}(\boldsymbol{r}) \tag{51}$$

The nuclei have a huge mass compared to the electrons. As a result, the speed at which the electrons move is much higher relative to the cores. Therefore, the electron positions may be altered while the nucleuses are kept in place. Meaning that the electron wavefunctions may be calculated assuming constant nuclei positions, resulting in a simplified equation:

$$\hat{H} = T_e(\boldsymbol{r}) + V_{Ne}(\boldsymbol{R},\boldsymbol{r}) + V_{ee}(\boldsymbol{r}) \tag{52}$$

Density functional theory

Even though the Hamiltonian (52) has been significantly simplified from (51), it is still a big challenge to calculate the electron movements and potentials of even simple structures. This problem was circumvented by Hohenberg and Kohn [24]. Their first theorem states that for a given external potential $V_{ext}(\boldsymbol{r})$ there can only exist a single ground state electron density $n_0(\boldsymbol{r})$. The theorem also states that any ground state property of the material can be described as a function of the ground state electron density $n_0(\boldsymbol{r})$.

The second Hohenberg-Kohn theorem states that the ground state energy of the system can only be the ground state if, and only if the input electron density is the ground state density. Where the energy is given by the coulomb electron-electron:

$$E\big(n(\boldsymbol{r})\big) = T_e\big(n(\boldsymbol{r})\big) + E_{ee}\big(n(\boldsymbol{r})\big) + E_{ext}\big(n(\boldsymbol{r})\big) = F_{HK}\big(n(\boldsymbol{r})\big) + E_{ext}\big(n(\boldsymbol{r})\big) \tag{53}$$

$F_{HK}(\boldsymbol{r})$ is the Hohenberg-Kohn functional and includes the electron-electron interaction and kinetic energy. As the external potential and its energy $E_{ext}\big(n(\boldsymbol{r})\big)$ is given by the structure of the material the million-dollar question of DFT lies in the form of $F_{HK}(\boldsymbol{r})$. The coulomb interactions between the electrons $J(n(\boldsymbol{r}))$ is known and the remaining part of the electron-

electron interaction is the non-classical $E_{ncl}\big(n(\boldsymbol{r})\big)$. The Hohenberg-Kohn functional is therefore rewritten as:

$$F_{HK}(\boldsymbol{r}) = T_e\big(n(\boldsymbol{r})\big) + J(n(\boldsymbol{r})) + E_{ncl}\big(n(\boldsymbol{r})\big) \tag{54}$$

Later Kohn and Sham found that a large part of the electrons kinetic energy could be accurately described by defining a non-interacting reference system, consisting of single electron orbitals that do not interact, though having the same electron density as the real system. The non-interacting kinetic energy is labelled $T_s\big(n(\boldsymbol{r})\big)$. While the rest of the real kinetic energy is defined as an unknown functional $T_c\big(n(\boldsymbol{r})\big)$.

$$T_e\big(n(\boldsymbol{r})\big) = T_s\big(n(\boldsymbol{r})\big) + T_c\big(n(\boldsymbol{r})\big) \tag{55}$$

Exchange and correlation approximations

An exchange correlation energy is defined as:

$$\begin{aligned} E_{XC}(n(\boldsymbol{r})) &= \Big(T_e\big(n(\boldsymbol{r})\big) - T_s\big(n(\boldsymbol{r})\big)\Big) + \Big(E_{ee}\big(n(\boldsymbol{r})\big) - J(n(\boldsymbol{r}))\Big) \\ &= T_c\big(n(\boldsymbol{r})\big) + E_{ncl}\big(n(\boldsymbol{r})\big) \end{aligned} \tag{56}$$

The energy is cleverly defined as such to include all the unknown contributions. The only endeavour then, is to find an approximate for $E_{XC}(n(\boldsymbol{r}))$. The solution of Kohn and Sham to this problem was initially the local density approximation (LDA). Assuming that the real exchange correlation energy can be equal to the contribution from a free electron gas of identical density. Though, only assuming a localized constant electron density. Though this approach works poorly for systems in which the electrons greatly deviate from a free electron gas.

The general-gradient approximation (GGA) came as an improvement to the LDA during the eighties. Instead of only assuming a constant localized electron cloud one may additionally add the gradient of the electron density in a Taylor expansion. Thus, improving the computational accuracy for un-homogeneous electron clouds. The GGA is a collective name for functionals applying this method, one such functional which is often used in materials science is the PBE functional developed by Perdew, Burke and Ernzerhof [25]. For the calculation of $BaZrO_3$ a variant of the functional, PBE revised for solids (PBEsol) [26], can

be used. The PBEsol shows excellent results for binding energies in ionic materials and delivers more accurate bulk moduli and lattice constants. Which in turn is essential for strain calculations.

3 Literature

3.1 Proton conducting perovskites

Iwahara and Takahashi early on began a systematic investigation of proton conducing oxides, initially focusing on perovskite type cerates [27-29]. Early studies of strontium cerates showed high hole conduction in dry conditions and proton conduction in a wet hydrogen containing atmospheres. Therefore, they suggested the equilibrium between H_2O and O_2 (57) as the protonation mechanism [28].

$$H_2O(g) + 2h^{\bullet} = \frac{1}{2}O_2(g) + 2H^{\bullet} \tag{57}$$

Later studies by Iwahara and others [9, 15, 29] however strongly suggest that the protonation of oxides in humid atmosphere happens by the consumption of oxygen vacancies following equation (5). Iwahara et al. later became the first to confirm proton conduction in acceptor doped $BaZrO_3$ under a hydrogen rich atmosphere [30]. The perovskite type materials have become one of the most promising electrolyte materials for PCFC applications because of both high chemical and mechanical stability. While other materials such as perovskite type cerates, many of which exhibit great hydration, are prone to degradation in CO_2 and/or H_2O containing atmospheres [7].

The water uptake of perovskites has been thoroughly investigated by Kreuer et al., as shown in (Figure 10) for acceptor doped barium zirconates. They further measured the he hydration rate of $BaZr_{0.9}Y_{0.1}O_3$ at 450 ℃ to be ~ 70 % [31]. Meaning that under such conditions some other positive defects, namely holes and oxide ion vacancies must charge compensate the remaining acceptors such that $[Acc] - [OH_O^{\bullet}] = 0.03 \ = 2[v_O^{\bullet\bullet}] + h^{\bullet}$. In PCFC operating conditions in reducing humid atmospheres around 450 ℃ the hole concentration and oxide ion mobility is low, and protons are the only significant charge carrier [32]. In dry atmospheres however, holes are assumed to be the dominating charge carrier according to equation (6). In the work of Bohn [32] no pO_2 dependence is found for the conductivity of BZY under humid conditions. However Nernst voltage measurements by Schober and Bohn [33] show low ionic (O^{2-}, H^+) transport numbers $0.05 - 0.07$ under humid oxidizing conditions. While under humid reducing conditions an ionic transport number of 0.97 ± 0.03 was measured in a temperature range down to 400 ℃.

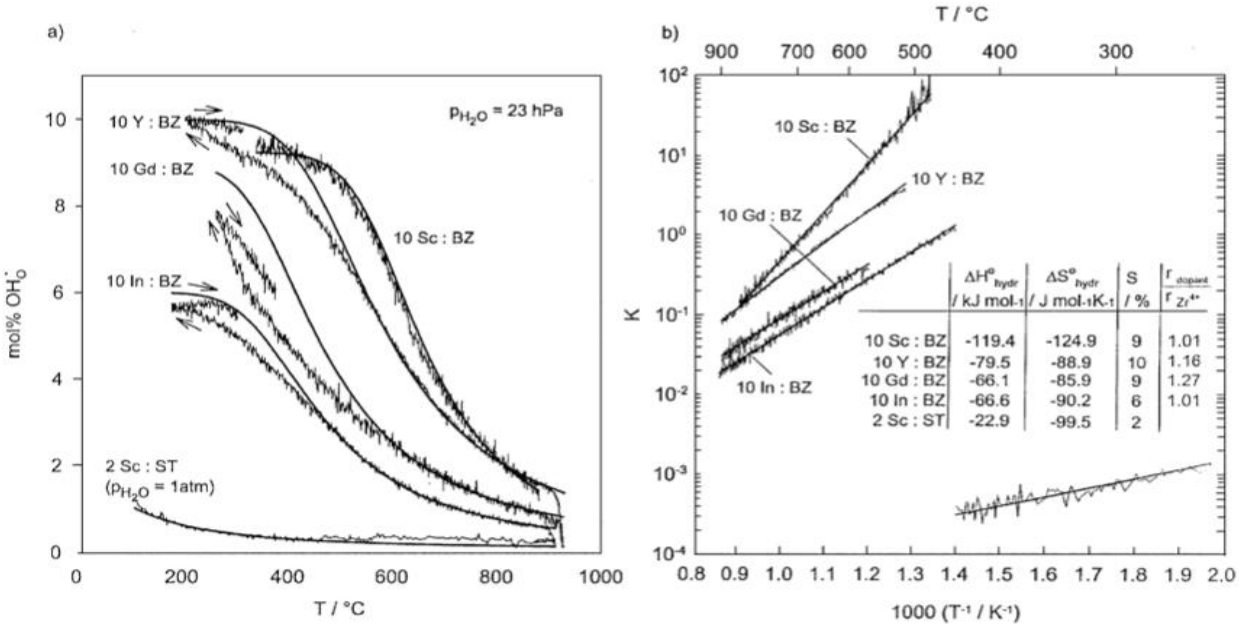

Figure 10. a) The hydration rate of acceptor doped barium zirconates and b) Arrhenius plots of the hydrations with the experimental thermodynamic data in the legend. Image borrowed from Kreuer's paper [7].

Proton trapping

Several computational works from 2004 and onwards by Björketun, Stokes and Islam have shown that the long-range proton mobility in acceptor doped $BaZrO_3$ and other perovskites is affected by the dopant-proton interactions [34-38]. The proton sites in close vicinity to the acceptor dopants are lower in energy, acting as energy wells efficiently trapping protons. Early IS conductivity and neutron scattering measurement found no clear evidence of the trapping behaviour however [39, 40]. Arguing that the measured activation energies from neutron scattering measurements might not be sufficiently localized to give rise to two different proton environments, which if present would lead to trapping effects.

While Islam and Stokes [34, 38] only examine the nearest neighbouring (1NN) dopant-hydroxide association energy in their calculations, Björketun found that for Y-doped $BaZrO_3$ the 1NN and second nearest neighbouring (2NN) hydroxide-dopant sites are almost equal in energy, the 2NN site being slightly more stable by $-0.01\ eV$ [37]. The protons are thus trapped at the two sites. The protons were found to be freed from the energy well after rotating away from the dopant while on the 2NN site. Takahashi et al. investigated the proton-proton interactions with respect to the proton-dopant distance. Similarly to Björketun, they found that the second nearest neighbouring positions were the most stable in BZY, both for isolated and associated protons [41].

In 2013 Yamazaki et al. presented experimental evidence that proton trapping actually is hindering long range proton transport [12]. The association reaction of yttrium-dopants and protons in BZY (58) is exothermic, leaning towards the product side at lower temperatures. *f* subscript denotes a free defect.

$$OH_{O,f}^{\bullet} + Y_{Zr,f}^{/} = \left(OH_{O}^{\bullet} Y_{Zr}^{/}\right)^{x} \tag{58}$$

The equilibrium is suggested by Yamazaki et al. to undergo a transition at 700 K from trapped to trap-free protons. This can be seen experimentally as a reduction of the gradient in an Arrhenius plot. At high temperatures the apparent long-range diffusivity approaches the trap-free diffusivity, calculated by Yamazaki et al. A modified diffusivity equation for mobile species exposed to trapping sites is suggested

$$D_{app} = D_0 \frac{\exp(-E_a/RT)}{1 + \left[Y_{Zr,f}^{/}\right] A(-E_{as}/RT)} \tag{59}$$

where E_{as} is the association energy of equation (58), *A* the preexponential factor and D_{app} is the apparent diffusivity from measurements. An in dept explanation can be found elsewhere [12]. This is supported by neutron spin-echo experiments by Karlsson et al. [40]. Their measured short range proton diffusivity matches the calculated trap-free diffusivity. A similar trapping mechanism is found for the oxide ion vacancy mechanism in STS in a computational study by Schie et al. [42]. They find that the activation energy strongly decreases when entering a high temperature trap free regime.

Table 1. Bulk activation energies E_a and association energies E_{as}

System	E_a /eV	Reference, method	System	E_{as}/eV	Reference
BZO	0.69	[43], calc	BZY	0.26	[34], calc
BZY20	0.47	[12], TG, IS, pe	BZY20	0.30	[12], calc
BZY	0.44-0.46	[44], IS, pe	BZY3.7	0.16	[37], calc
BZY10	0.43	[7], IS, pe	BZY1.6	0.23	This work, calc

BZY10	0.63	[11], IS, tf
BZY10	0.51	This work, IS, tf
STF10*	0.7	[45], IS, pe
STF0.01*	0.63	[46], single crystal

TG, Thermogravimetry; IS, Impedance spectroscopy; calc, calculated; pe, pellet sample; tf, thin film sample.
* Fe doped $SrTiO_3$,

Thin film barium zirconate

Typical reported bulk conductivities of BZY range from 0.1 to 30 mS/cm at 450 ℃ [7, 47, 48]. The bulk conductivities are measured from polycrystalline pellets from the high frequency response of IS conductivity measurements. The total conductivities are however much lower due to resistive grain boundaries [9]. Several studies of nano-grained thin film BZY deposited by sputtering and chemical solution deposition show comparable or higher bulk and total resistances compared to sintered pellets [47, 49].

Shim, Gür and Prinz [44] reported very high proton conductivity in epitaxially BZY grown onto a MgO (001) substrate for the first time in 2008. The films having an activation energy of around 0.45 eV which is in the range of bulk measurements (Table 1). Additionally, films deposited onto an amorphous quartz substrate resulted in polycrystalline and highly resistive samples, $10^4 - 10^6$ times higher resistance compared to films deposited onto MgO.

Pergolesi et al. published in 2010 a record high protonic conduction in 20 % Y-doped BZO measured by IS [11]. The films were fabricated by pulsed laser depositing of the doped barium zirconate onto a single crystalline MgO substrate. The achieved total conductivity of 0.11 Scm^{-1} at 500 ℃ was two orders of magnitude higher than earlier reported total conductivities measured on sintered pellet samples. In contrast to the work of Shim et al. who achieved enhanced proton conductivity by decreasing film thickness below 110 nm. The improved conductivity assumed by Shim et al. to be the result of improved crystallinity at lower film thicknesses. Pergolesi et al. report single crystalline 1 μm thick films. Interestingly the films of Pergolesi et al. experience no dehydration up to 600 ℃, while the isobars of K. D. Kreuer clearly show dehydration around 400 ℃ of BZY10 (Figure 10). Interpolating bulk conductivities deconvoluted from polycrystalline pellets agree with the total conductivity of the thin film. H_2O/D_2O isotope exchanges further confirm proton

conduction, supporting the claim that the high conductivity stems from proton conduction, and not holes.

The grain boundary cores have been shown to have high oxygen vacancy concentrations acting as highly resistive proton barriers [50]. The space charge zone around the core is depleted of protons and other positive defects, and as a result of the positive gb core the concentrations of negative defects increase. As a result, the activation energies of grain boundaries are higher than the bulk activation energies [7].

High sintering temperatures in combination with the volatile barium often results in a Ba deficiency in $BaZrO_3$ samples [51]. The deficiency is shown to result in a degradation of the protonic transport properties, proposed to be a result of dopant substitution on the A site in addition to the B site and increased grain boundary density and resistance over individual grains.

3.2 Heterostructure engineering

Nano engineering has proven to be a strong tool to control materials properties [19, 20, 52]. The materials microstructure greatly affects the functional properties, and therefore is heterostructure engineering important for advancing materials science.

Deposition and structure

Mi et al. [53] achieve epitaxial growth of a BZO/STO layered thin film onto a MgO substrate by a RF-sputtering technique. Subsequent high-resolution TEM show that the MgO/BZO interface is characterized by two interface types, a MgO/ZrO_2 type and MgO/BaO type. Both interface types grown with a cube-on-cube relationship. The BZO/STO interface contains a high density of misfit dislocations owing to the large lattice mismatch of 7 % (Table 2).

MgO has a tendency to react with atmospheric air to create hydroxide groups at the surface which is unfavourable for epitaxial film growth [54]. Annealing at high substrate temperatures around $700\,℃ - 800℃$ has been shown by Febvrier et al. to be an effective method for removing hydroxide and carbonates from the MgO surface [55]. Febvrier et al. further discuss the effect of substrate wet cleaning as a means to remove surface groups on the MgO prior to deposition. The wet cleaning methods was found to have a large impact the cleanliness of the surface, sonication in detergent followed by solvent cleaning reduced

surface group concentrations and improved deposited film quality. High pO_2, above $0.133\ mbar$ during PLD of BZY onto a MgO substrate produce poor quality films with low proton conduction [56].

MgO, BZO and STO have well matching lattices allowing for epitaxial growth. When yttrium doping barium zirconate however, the perovskite adapts a slightly tetragonal structure [7]. At high doping levels $> 20\%\ Y$ the perovskite reverts back to its cubic symmetry. Additionally, BZY20 has a lattice constant closer to MgO than the undoped BZO.

Table 2. Structural data at 25 ℃

Material	Symmetry	Lattice constant (Å)	Reference
BZO	Cubic, $Pm\bar{3}m$	$a = 4.192$	[57]
BZY10	Tetragonal, P4mm	$a = 4.215$, c = 4.205	[7]
BZY25	Cubic, $Pm\bar{3}m$	$a = 4.216$	[7]
MgO	Cubic, $Fm\bar{3}m$	$a = 4.190$	[58]
STO	Cubic, $Pm\bar{3}m$	$a = 3.905$	[59]
STS5	Cubic, $Pm\bar{3}m$	$a = 3.908$	[2]

Several studies have shown a strong correlation between BZY film thickness and quality, higher thicknesses resulting in reduced quality [44, 60, 61]. Thick films are characterized by a rougher surface and lower conductivity. The latter hypothesized to be a result of defect formation to relax the BZY lattice strained by the MgO substrate.

Space charge

Any structural changes in a periodic lattice might be accompanied by chemical changes. The segregation energies of $OH_O^{\bullet}$ and $v_O^{\bullet\bullet}$ defects have been calculated by Saeed et al. using DFT for STS and BZY (Figure 11). Because of different lattice constants the STS and BZY cannot be modelled in a single supercell as the large strain (7 %) results in unwanted artifacts.

Therefore, the two systems are modelled separately. The Gibbs formation energy equation used to calculate the segregation energy of the defects follows:

$$\Delta_f G_{def} = E_{def}^{el} - E_{bulk}^{el} + \Delta_f G_{def}^{vib} - \sum_i \Delta n_i \mu_i(T,p) + q(\varepsilon_{VBM} + \varepsilon_F + \Delta\varepsilon) \quad (60)$$

E_{def}^{el} and E_{bulk}^{el} is the total energy of the defect containing and pure supercell respectively. $\Delta_f G_{def}^{vib}$ contains the vibrational energy change, and μ_i and Δn_i are the chemical potential and change in number of atoms i respectively. The last term contains the effective charge q, fermi level ε_F, the difference in valence band minima ε_{VBM} (calculated as the difference in ionization potential between the two materials) and a term $\Delta\varepsilon$ to correct for the change is band edges. The segregation energy of $OH_O^\bullet$ and $v_O^{\bullet\bullet}$ calculated to be -0.56 and -0.64 eV respectively calculated according to

$$OH_{O,STS}^\bullet + O_{O,BZY}^x = OH_{O,BZY}^\bullet + O_{O,STS}^x$$

for $OH_O^\bullet$ and similarly for $v_O^{\bullet\bullet}$. Integrating the $OH_O^\bullet$ concentration 2.5 nm from the interface into the BZY layer the concentration is found to increase by ~50 % on average.

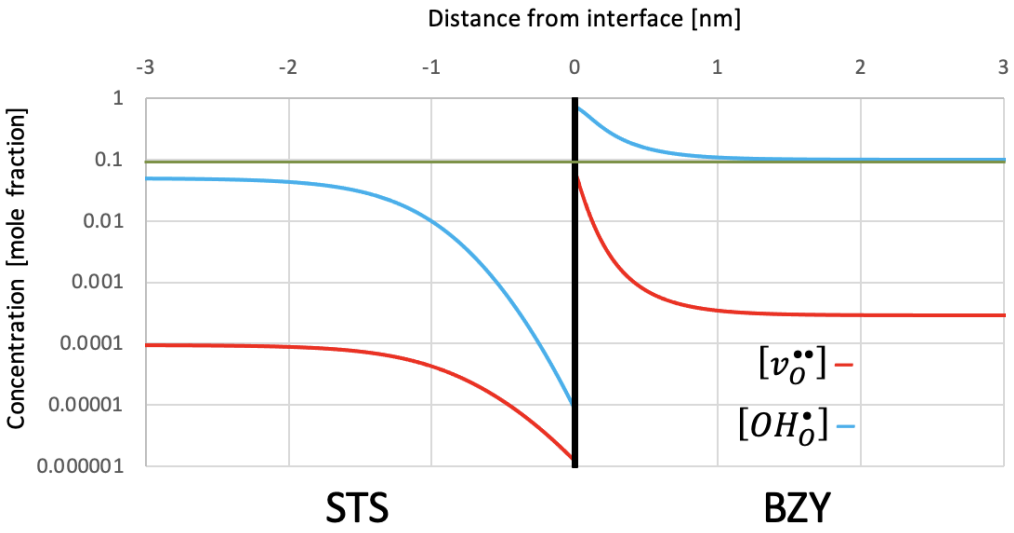

Figure 11. Defect concentrations around the STS10/BZY10 interface (black vertical line) and the green line indicates the acceptor concentration at 600 ℃ [14].

Strain

Kreuer et al. found that the perovskite type structures with a higher lattice constant had a tendency to show a higher proton conductivity [9]. Similarly, the computational and

experimental work of Fluri et al. that by increasing a biaxial lattice of BZY results in higher proton mobility [1]. Compressive strain on the other hand reduced proton mobility. Experimental strain was applied by PLD epitaxial growth on substrates with different lattice constant. DFT calculations show that the tensile strain increases the O-O distance but also reduces the dopant-proton association energy. Thus, the tensile strain reduces the long-range proton transport activation energy.

In a molecular dynamics study by Ottochian et al. they find that the proton conductivity on the contrary increased under compressive strain [62]. Part of the effect was attributed to the decreased O-O distance, which again would decrease the jumping distance of the migrating protons. However, they do not take into consideration the dopant-proton association.

Saeed, Norby and Bjørheim found in a computational study [14] that strain can affect the formation energy of hydroxide defects and oxygen vacancies. Compressive strain was found to increase the hydration energy while tensile strain decreases it. Negative defect formation volumes are generally stabilized by compressive strain which agrees with $OH_O^{\bullet}$ having a formation volume of -4 Å^3.

Layered films

A recent paper by Ngabonziza et al. [13] investigate a novel strategy of 2D doping by epitaxial deposition of BZO/$BaYO_{3-x}$ films. The films achieve appreciable conductivity comparable to the bulk conductivity of BZY10 measured by Schober [63]. By doping one unit cell thick layers parallel with the conduction path of the protons the authors suggest that the geometry allows for percolating pathways for proton conductivity. However, as mentioned by Ngabonziza et al. a high Y-concentration has been found to decrease proton mobility by creating stronger trapping sites for protons neighbouring two or three Y ions. Their trapping energies calculated by Draber et al. to be $0.37 - 0.55\ eV$ and $0.66\ eV$ respectively, compared to $0.22 - 0.35\ eV$ for protons neighboring one Y ion [64].

DFT papers generally agree that the nearest neighbouring (1NN) Y-proton position and the second nearest neighbouring position (2NN) are the most stable. [65, 66]. The protons were found most stable pointing towards the Y-dopant, giving a Y-H^+ distance of 2.3 and 3.9 Å at the 1NN and 2NN positions respectively. Torayev et al. [65] show that even for protons situated at the same oxide ion, their energy depends on what direction the proton pointing relative to the Y-dopant.

Table 3. Enthalpy and entropy of hydration

Material	ΔH^0_{Hydr} / $kJ \cdot mol^{-1}K^{-1}$	ΔS^0_{Hydr} / $J \cdot mol^{-1}$	Reference, method
BZY10	-79.5	-88.9	[7], TG
BZY10	-74	-9	[33], TG
BZY3.7	-76	-	[37], calc
BZO	-74	-	[67], calc
BZO	-63.6 – -69.0	-	This work, calc

TG, thermogravimetry; calc, calculated.

4 Experimental

4.1 Sample preparation

10 % Y-doped $BaZrO_3$ and 10 % Sc-doped $SrTiO_3$ supplied from CerProTec were cold pressed into 20 mm diameter pellets and sintered to 1600 °C in ambient air and were later used as targets in the PLD. BZY and STS will from here on refer to 10 % Y-doped $BaZrO_3$ and 10 % Sc-doped $SrTiO_3$ respectively. The same targets were used for all samples, both deposited in this work and by Dr Saeed. The substrates used were single crystalline MgO (001) 1 cm^2 plates manufactured by Crystal GmbH. The substrates have been polished on one side, giving a very even surface with 90 % of the surface within ± two unit cells, as measured by atomic force microscopy by the manufacturer. Most of the substrates used were cut into four even squares (5×5 mm) or two rectangles (10×5 mm) using a diamond tipped cutter.

PLD

Pulsed laser deposition (PLD) was used to deposit the materials onto a substrate. A. SURFACE integrated PLD-workstation was used, including a COMPexPro™ 201F (Coherent®) 248 nm KrF excimer laser to ablate the target material.

The high-powered pulse from the laser hits the target and the electromagnetic radiation absorption of the material surface leads to rapid heating and evaporation of the material which spreads in a plume. Because of the rapid heating the material stoichiometry is conserved. The target holder rotates during deposition to ensure even ablation of the target, and alternating films can easily be fabricated as the vacuum chamber is equipped with four target holders. Ag conductive ink (Liquid S-020, Alfa Aesar) is applied to the metal holder and the target and dried for 15 minutes at 160 ℃, working both as an adhesive and as a thermal contact.

Final optimized depositions were performed by heating the substrate to 750 ℃ and depositing the film while the substrate maintains the temperature. The laser intensity was set to 1,8 mJ/cm^2 (450 mJ) at a shot frequency of 5 Hz. The growth rate was found to be approximately 0.33 Å per shot. During the deposition the target is rotated at 60 rpm while the ambient pressure in the chamber was maintained at 0.05 mbar of O_2. Initially, the chamber is

pumped down to a base pressure of $5 \cdot 10^{-5}$ mbar. Subsequent heating and cooling were performed at 5 °/min at $7 \cdot 10^{-3}$ mbar of O_2. The film series TF-11 to TF-18 (A 1) were deposited using this procedure.

Depositions were tested out using a number of different specifications, varying pulse frequency, substrate to target distance, pAr to pO_2 background gas, number of shots, and pre deposition wet cleaning. Film series TF-1 to TF-10 (A 1) were deposited under such varying conditions.

Electrode preparation

Several electrode variants of different composition and preparation method were applied onto the thin films. The simplest variant included painting a thin layer of Ag paste onto the thin films and attaching Pt current collectors to them. Thereafter the electrodes were dried for 15 min in a heating cabinet at 160 °C. To improve the electrolyte-electrode contact area an Ag target was ablated by PLD onto the thin film. A metal mask shaded a 1 mm thick strip of the film during the metal deposition. Ag paste was thereafter applied as described beforehand.

Lastly Pt deposition was also performed using electron-beam deposition (Ångstrøm instrument). An electron beam was accelerated by a voltage of 7.8 kV at around 300 mA to ablate Pt at a deposition set rate of 0.5 Å/s. Samples were partially covered by metal masks, both simple parallel strip electrodes and interdigitated electrodes with a 1 mm slit. A thin layer of Ti was initially deposited as it has better adhesive properties, while the Pt layer protects the Ti from oxidation during high temperature measurements. Ag paste was used to cement the Pt wires to the electrodes.

4.2 AC measurements

Apparatus

All measurements were carried out in a Probostat (Norecs), a tubular gas thigh electrochemical measurement setup. The Probostat is set up for four wire, two-point measurement. The wires were of Pt and were twined with the sample current collector Pt wires. Gas in and outlets allow for control of the atmosphere and a Pt/(Pt 10 % Rh) thermocouple situated right beside the sample was used to monitor the temperature. The thermocouple and outer steel tube are grounded in order to minimize electric fields affecting

the measurement, which is necessary due to the high resistivity of the thin films. The four independent shields for each of the four electrode connects were not interconnected as the potentiostat supports driven shield technology.

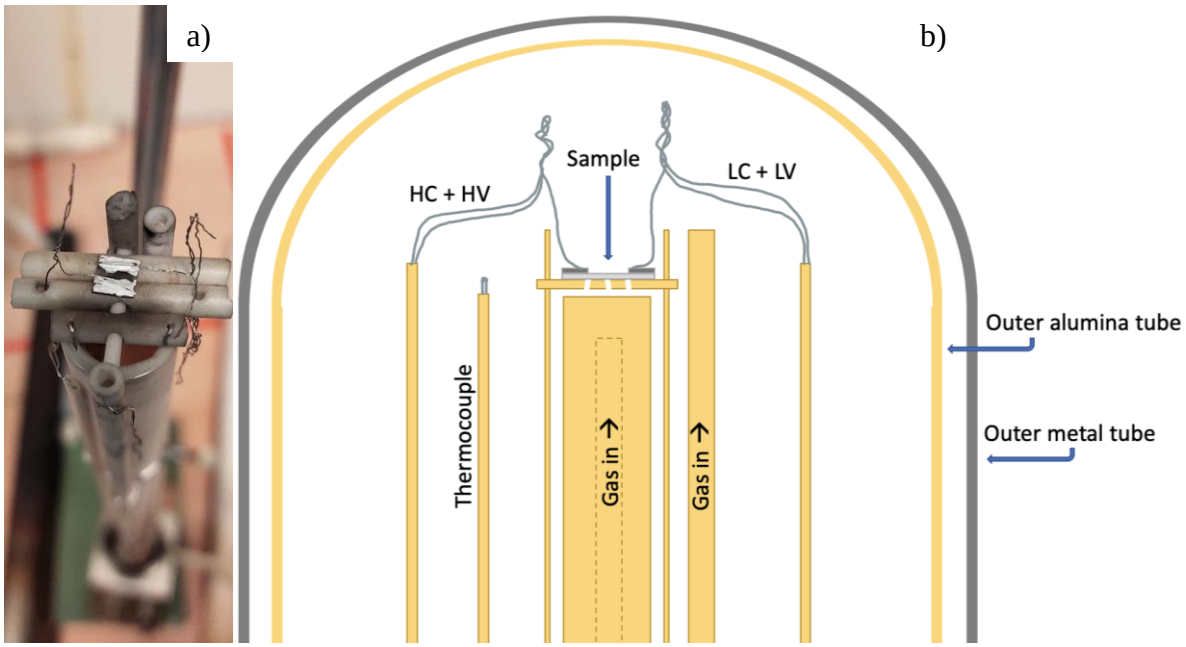

Figure 12. Electrochemical measurement setup diagram (top part) b) and picture of sample FI-7 a) (Y-doped $BaZrO_3$ thin film with ag paste electrodes).

The Probostat was inserted vertically into a tubular furnace. A 4-wire impedance test interface was connected to the Probostat using 20 cm long cables, kept short to reduce inductive contributions. The test interface was further connected to the potentiostat (Alpha-A frequency analyser, Novocontrol Technologies). The voltage channel input of the test interface has an impedance of 10^{12} Ω and capacitance of 10 pF.

A gas mixer was used for supplying oxidizing, inert or reducing atmospheres ranging from pure oxygen to 5 % hydrogen. The gas mixer features a drying stage, a H_2O and D_2O wetting stage. The wetting was performed by passing the gas over a water container before bubbling through KBr saturated water, resulting in approximately 80 % relative humidity. The drying of the gas was performed by passing it over P_2O_5 powder, which according to the manual values [68] result in a $pH_2O < 10^{-6}$.

The Progasmix software (Norecs) was used for calculation of partial oxygen pressures. The gases supplied are from Nippon Gases, the Ar gas having a 99.999 % purity and assumed to have $pO_2 = 10^{-5}$ bar. The gas mixer setup is presented below in (Figure 13).

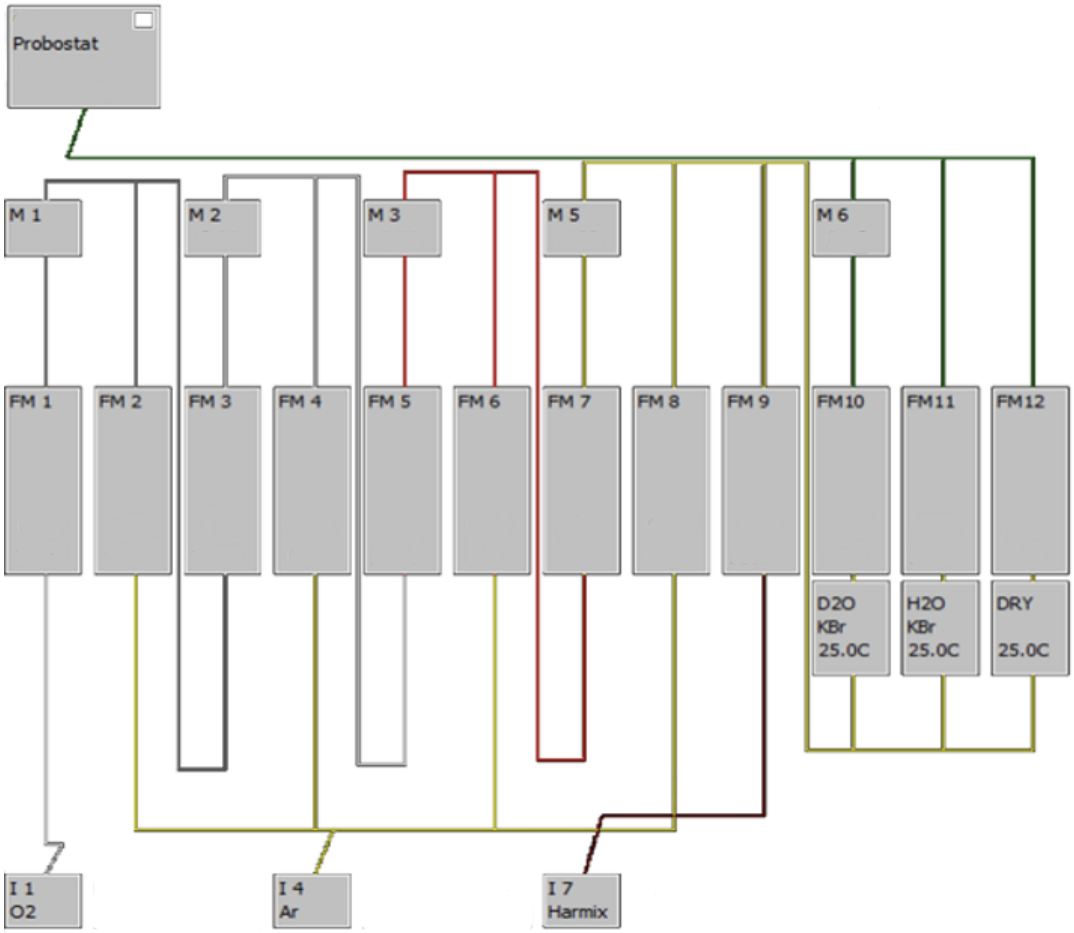

Figure 13. Gas mixer diagram. Three input gases supplying the flowmeters and gas mixes, abbreviated FM and M respectively. Two-stage wetting by first passing the gas through a water containing beholder followed by bubbling through KBr containing water.

Conductivity measurements

AC impedance sweeps were performed mainly at the frequency range from 1 MHz to 1 Hz, but for highly resistive samples frequencies down to 0.01 were necessary in order to plot a full semicircle in the Nyquist plot. Constant frequency measurements as a function of time were performed at appropriate frequencies adapted to each sample. The wave amplitude was 1 V. A high potential reduces the measurement noise, and the results were found to be unaffected by the potential used. Samples were equilibrated until the constant frequency conductivity flattened out appropriately.

Activation energies were measured from 600 ℃ down to 150 ℃ at 50 ℃ steps. Below 350 ℃ the proton concentration is assumed to be frozen in during the relatively short time frame of the measurement, meaning that the activation energy of the mobility could be

properly extracted. The activation energy is found from Arrhenius plots (Figure 14) of $ln(\sigma T)$ versus *1/T* from equation (24) as:

$$E_a = -gradient \cdot k_B \tag{61}$$

However, the Arrhenius plots in this thesis are presented with $log(\sigma)$ along the x-axis instead of $ln(\sigma T)$ as only the former is intelligible.

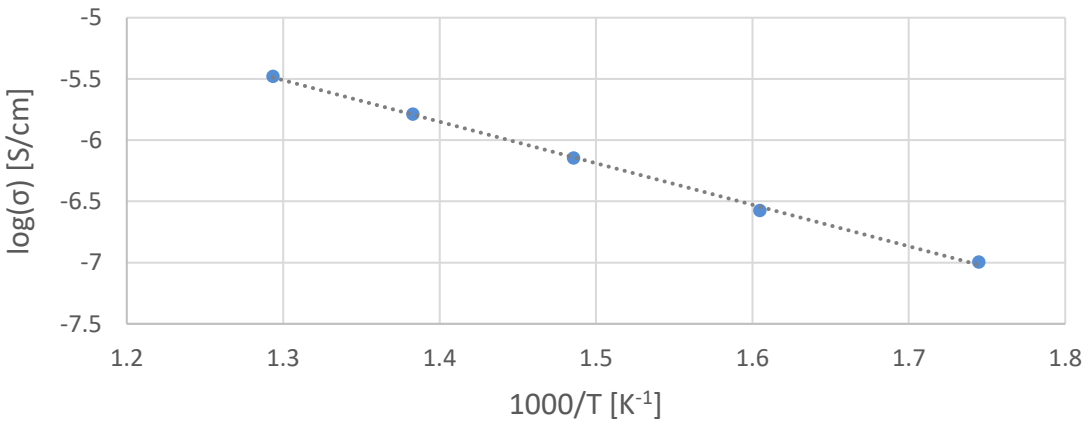

Figure 14. An Arrhenius plot showcasing the bulk conductivity of a $BaZrO_3$ thin film. The markers show the measurement data, while the dotted line is a linear regression of the data points. The regression line is only to indicate the linear behaviour and may not be used in this form to extract the activation energy.

The data was analysed using the Omega software (Norecs) and deconvoluted using ZView (Scribner Associates, Inc.). A Microsoft Excel sheet was used for simple calculations and plotting of e.g., Arrhenius's plots and a python script (Python 3.8) was used to plot the time dependent measurements.

The Novocontrol used for measuring experienced trouble maintaining a stable current at high frequencies above approximately 40 kHz (A 1) and the frequency range was not evaluated for the thin films.

The geometric correction for the conductance and capacitance was performed by assuming a rectangular electrolyte geometry. The length *L* being the distance between the electrodes, and the cross-section area *A* the thickness of the film multiplied by the width of the sample. The conductivity is then calculated from the deconvoluted resistance R_p as:

$$\sigma = {R_p}^{-1} \cdot \frac{L}{A}$$

4.3 Characterization

XRD

Before measuring the films were investigated by x-ray diffraction in a Rigaku MiniFlex600 tabletop XRD. Data analysis was performed in diffracEVA (BRUKER software). Measured from $10\,°$ to $90\,°$ using a $0.02\,°$ step length at $10\,°/min$. Instrument settings: $0.625\,°$ divergence slit, radiation voltage $40\,kV$ and current $15\,mA$. The thin film samples were attached to the sample holder by a piece of laboratory gum and levelled by gently pushing the thin film into the gum with a clean glass plate. The pellets used as targets were simply attached to the XRD sample holders using carbon tape.

SEM

Scanning electron microscopy was performed post measurements, mainly to check film thickness and look for grain boundaries The films were broken in two by hand and the cross section was then positioned towards the electron beam of the instrument (Quanta FEG 200, FEI Company). The imaging was done at $8 \cdot 10^{-4}$ Pa chamber pressure with a $20\,kV$ electron beam. The "stigmator", beam shift, gun tilt and lens alignment were optimized to improve imaging quality. However due to the resistive behaviour of the samples, charge quickly builds up along the surface during imaging which is detrimental to the image quality. Energy dispersive x-ray spectroscopy was not performed because of an instrument software failure.

4.4 Modelling

Calculations were all done on Saga, a supercomputer which is part of the Norwegian academic HPC infrastructure and maintained by the Sigma2 metacentre. The program used for DFT calculations was the ab-initio total-energy and molecular-dynamics program VASP (Vienna ab-initio simulation program) developed at the Institut für Materialphysik of the Universität Wien [69, 70]. The INCAR input file for the VASP program is found in the appendix (A 11).

DFT calculations were performed with plane wave expansions with the GGA in the PBEsol form. The electrons of the core were represented by ultrasoft pseudopotentials [70]. An automatically generated k-mesh following the Monkhorst-Pack scheme [71] with a gamma centred grid and a $2 \times 2 \times 2$ k-point sampling is used.

The number of cores working on each wavefunction $NCORE$ is usually set to an integer close to the square root of the number of cores. Though for the system $NCORE = 2$ was found to be the fastest. The number of cores was varied from 8 to 28 and a core number equal to 20 was found to give a high efficiency paired with low computing times. The plane wave cut-off energy was set to $550\ eV$ chosen as such by calculating the total energy with $50\ eV$ steps until the energy converged within $1\ meV$. Relative convergence tests were also performed by moving an oxide ion slightly off the equilibrium position. Geometric optimization for ionic positions and cell volume was performed with the constraint that the energy convergence be less than $10^{-5}\ eV$ for the self-consistent calculations.

Cells

$4 \times 4 \times 4$ cubic BZO and BZY1.6 supercells were constructed, for BZY the proton and Y defects were positioned at the 1NN position. The two supercells were relaxed twice with respect to both volume and ion positions. The initial relaxation was performed using a conjugate gradient algorithm. The second relaxation uses a quasi-Newton algorithm which is faster but had a tendency to fail for badly guessed proton positions if used in the initial relaxation. Afterwards an accurate total energy calculation was performed. Geometry optimization of other cells e.g., cells used for strain calculations was only performed relaxing ionic positions and not volume.

Strained cells were built by straining the cells in an ab-plane while allowing for relaxation in the c-direction. The strain was manually applied by fixing the axis values in the ab-plane and guessing the c-axis value. For the perovskite structure a compressed plane would mean that the octahedra will be elongated in the normal direction, and oppositely. Several guesses of the c-axis were made, and the total energy fitted using a second-degree polynomial to extrapolate the optimal c-axis value at the energy minimum.

Supercell correction

When adding a single defect to the supercell the number of electrons must be altered to correctly reflect the effective charge of the defect [72]. E.g., for a Y-dopant an electron must be added to the supercell while an electron must be removed from a H-dopant in order to create a proton. A homogeneous charge is therefore added to compensate for the defect, making the electrostatic potential of the defect supercell V_d different from the potential of the

undoped one V_u. The difference in electrostatic potential can be calculated by putting a test charge on an ion far from the defect in the defect supercell and compare it to a similar test charge in the undoped cell. The local potential at the test charge is calculated as:

$$V_{loc} = V_{ext} + \int \frac{n(\boldsymbol{r}')}{|\boldsymbol{r} - \boldsymbol{r}'|} d\boldsymbol{r}' + V_{XC}(\boldsymbol{r}) \tag{62}$$

The correction factor for the formation energy of defects of charge q can therefore be given as:

$$E_{corr} = q(V_d - V_u) \tag{63}$$

Association energies

Different association energies for different proton positions relative to the yttrium dopant was calculated for the 4x4x4 supercell doped with a single yttrium ion and one proton defect. The energies for five different proton-yttrium distances were calculated, from the nearest neighbour to an infinite distance.

The infinite separation association energy was calculated as

$$E_{as} = 2E_{Y,p}^{tot} - E_p^{tot} - E_Y^{tot} \tag{64}$$

where E^{tot} is the calculated total supercell energy. The subscripts from left to right denote the association energy, the energy of supercells with an Y and proton defect, only a Y defect and only a proton defect. Initially the three latter supercells were volume relaxed separately resulting in a large error of several eV. The energies were calculated by only relaxing the volume of the supercell containing both dopants, removing either of the dopants and performing an ionic relaxation, with or without added strain. Then, the lattice constants for the three differently doped cells are similar for each level of strain.

Hydration enthalpy

The formation energy for a defect can be calculated from the total energy of the defect cell E^{tot}(defect) and a perfect unit cell $E^{tot}(perfect)$:

$$\Delta E_{defect}^{tot} = E^{tot}(defect) - E^{tot}(perfect) \tag{65}$$

The formation energy of hydroxide defects from water vapor namely the hydration enthalpy E_{hydr} is calculated according to equation (66). The energy is calculated for undoped BZO only. The energy of the H_2O molecule $E_{H_2O}^{tot}$ is calculated by relaxing only atomic positions in a $20 \cdot 20$ Å supercell containing one molecule.

$$E_{hydr} = 2E_{OH_O^{\bullet}}^{tot} - E_{perfect}^{tot} - E_{v_O^{\bullet\bullet}}^{tot} - E_{H_2O}^{tot} \quad (66)$$

The subscripts $OH_O^{\bullet}$ and $v_O^{\bullet\bullet}$ denote the defects added to the perfect supercell. When calculating the hydration energy of BZY a Y dopant also is added to each BZO supercell.

4.5 Errors

The errors and uncertainties of this work has not been calculated. However, they must be assumed to be present and of significance.

The high frequency regime of the impedance sweeps includes a systematic error and is not included in the deconvolution, as discussed earlier. As a result, the reported resistances are overestimated by 1-2 %.

The PLD deposits films with greatly different properties even when the settings are identical. The largest failures are connected with vacuum pump failures, resulting in incorrect ambient chamber pressures during deposition. As discussed earlier, deposition pressure is important for film quality.

Flowmeter read offs of the gas mixer are inaccurate, giving rise to a $\pm$ 5 % uncertainty at each flowmeter. The gas mixer and measurement setup may be a source of gas leakages. The water vapor pressure after passing the dry stage of the gas mixer was found from empirical data by Norby and Kofstad to be 3 Pa [73], not < 0.1 Pa as given from the measurement setup manual [68].

5 Results

Four films of the BZO, BZY, BZO/STS and STS systems were successfully fabricated having a satisfactory conductivity and structure. The conductivity of the four films varied within one order of magnitude. In contrast to the poor BZY films of which the conductivity varied by up to four orders of magnitude, unoptimized deposition setting being the main reason for the large difference. A summary of all the films measured in this work can be found in the appendix (A 2). A comparison of the films measured at 450 ℃ in humid Ar, with identical thermal history, can be found in the appendix (A 3).

First the SEM and XRD characterization results are presented. Thereafter a conductivity measurement series at 450 ℃ where the conductivity is compared to different variables and systems. Thereafter conductivity dependencies of the temperature and atmosphere are shown. Lastly the results of three computational methods for calculating the trapping energy as a function of strain is presented.

5.1 Characterization

XRD analysis show that some of the films exhibit a polycrystalline structure, evident from the (110) peak found in some of the films Figure 16. As only the reflection planes parallel to the film surface should be reflected. Any other reflection planes thus correspond to tilted lattice. The films which do not have a visible (110) peak are assumed to be single crystalline. Generally, the thin films (60 nm) show single crystalline behaviour while the thicker films (1 μm) show polycrystalline behaviour.

SEM images show a well-defined thin film of approximately 1 μm (Figure 15). The real thicknesses are in good agreement with the nominal thickness estimated from the number of laser pulses. The film has a slightly uneven surface, which might be attributed to nanograin growth in the thick films. The Ag paste electrode which can be seen in the overview images, has peeled off slightly. Most Ag paste electrodes had reduced adhesion post measurements.

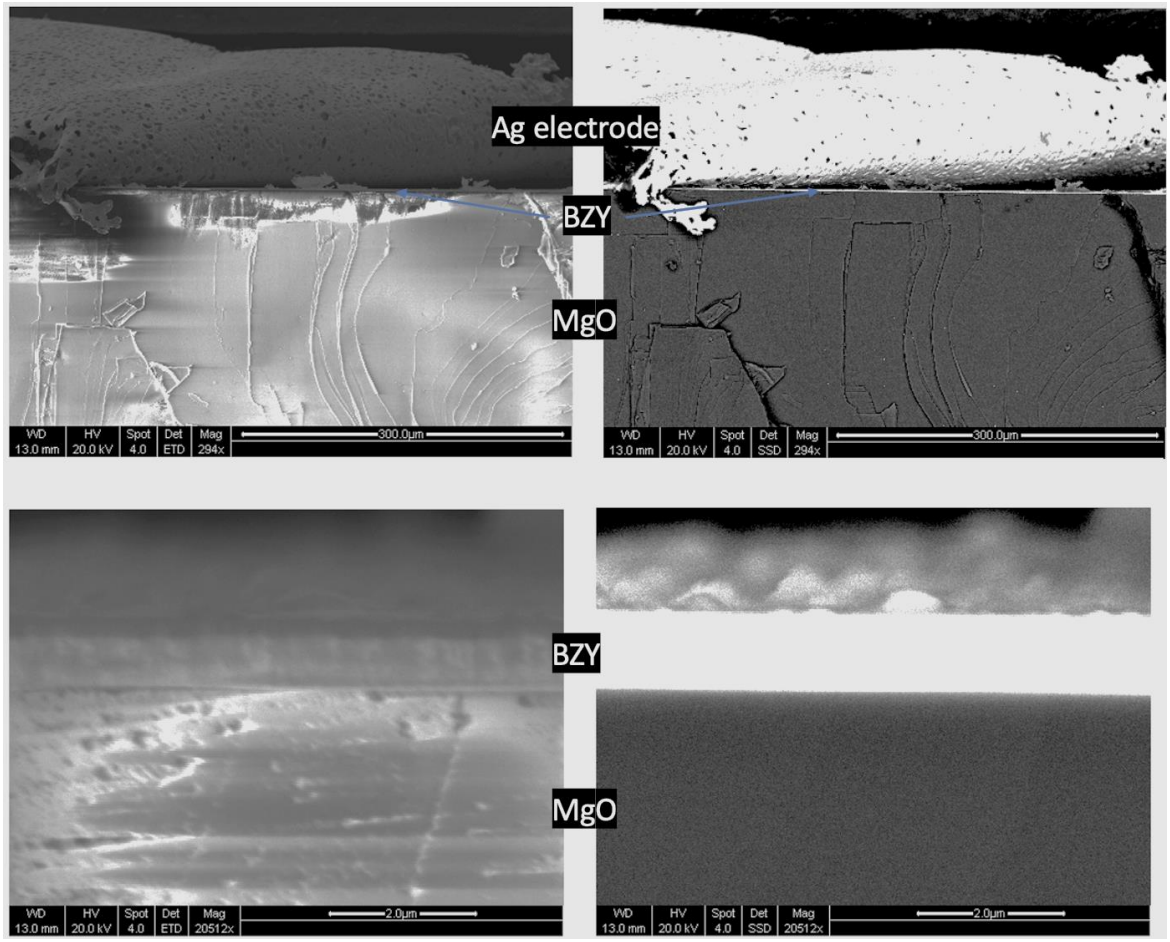

Figure 15. SEM images of a 1 μm thick BZY sample post IS measurements. Measured secondary electrons (left) and back scattered electrons (BSE) (right). The top images are for an overview, while the bottom images are close ups of the film. The heavier Ba and Zr atoms of the film are easily distinguished from the Mg of the substrate, the former appearing much lighter in the back scattered electron detector (right).

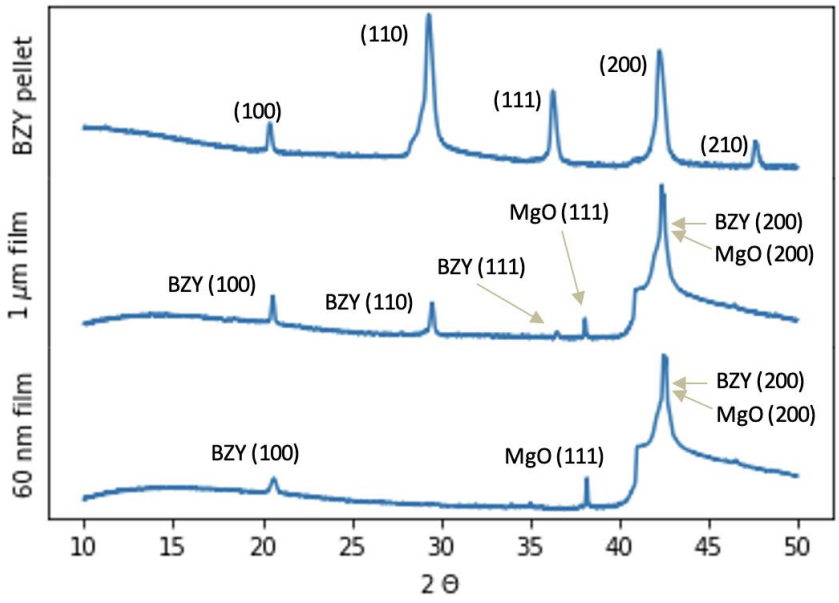

Figure 16. XRD spectra of BZY samples, namely the pellet used as a PLD target, a polycrystalline 1 μm thick film and a single crystalline film.

5.2 Impedance measurements

The reported conductivities are deconvoluted using the equivalent circuit described in (Figure 7). The fit was calculated according to the equations (39) and (40), illustrated in (Figure 17). The Nyquist plots all to a varying degree exhibit an impedance at high frequencies which cannot be attributed to the bulk, visible as a slight elongation. The elongation can be attributed to nanograins which don't manifest as an independent semicircle in the plot but is merged with the bulk semicircle.

The impedance of highly resistive samples is assumed to be dominated by the gb contribution as seen by a large impedance at lower frequencies (A 7). The polycrystalline samples were measured at low temperatures in order to separate the grain and bulk semicircles, however no degree of separation was achieved.

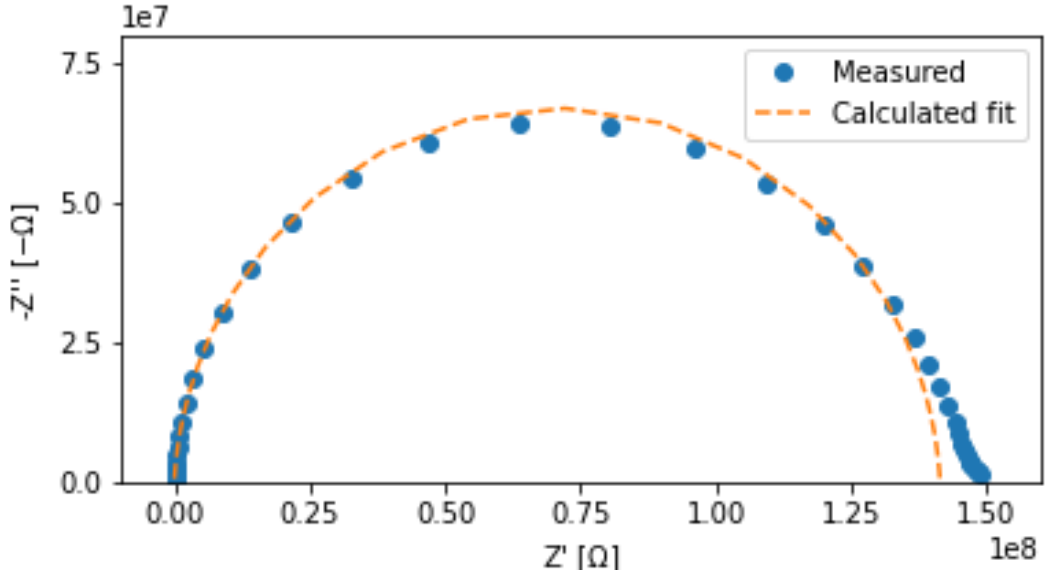

Figure 17. Nyquist plot of a BZY thin film, measured at 450 ℃ in humid Ar atmosphere. The rightmost measurement points not agreeing with the fit is assumed to be the gb contribution.

Constant temperature conductivity comparisons

To investigate the effect of nanoengineering several systems, namely BZO/STS, BZO/STO and BZO/BZY, are compared in terms of conductivity as a function of layer thicknesses of the heterostructure thin films (Figure 18). The conductivities presented are calculated from the total polarization resistance from IS measurements. There is no clear trend, but for all systems one or more of the heterostructures outperform the reference single phase films. Because of instability of the deposition technique, it is quite uncertain whether the

conductivity differences can be owed to the sample preparation or the materials heterostructure properties.

The BZO/STS heterostructure films exhibit conductivities in a relatively close range around the STS conductivity. The conductivity increase seen of some of these heterostructures might therefore not be solely attributed to a job-sharing process as much of the conductivity contribution comes from the STS. The BZO/STO heterostructures all conduct better than the reference films. The reason for the conductivity increase is uncertain but is assumed to be a result of strain or space-charge effects. The 2D doped BZO/BZY films show no clear trend. One of the heterostructure films exhibits a relatively high conductivity of 2.2 mS/cm, suggesting that the 2D doping method is feasible.

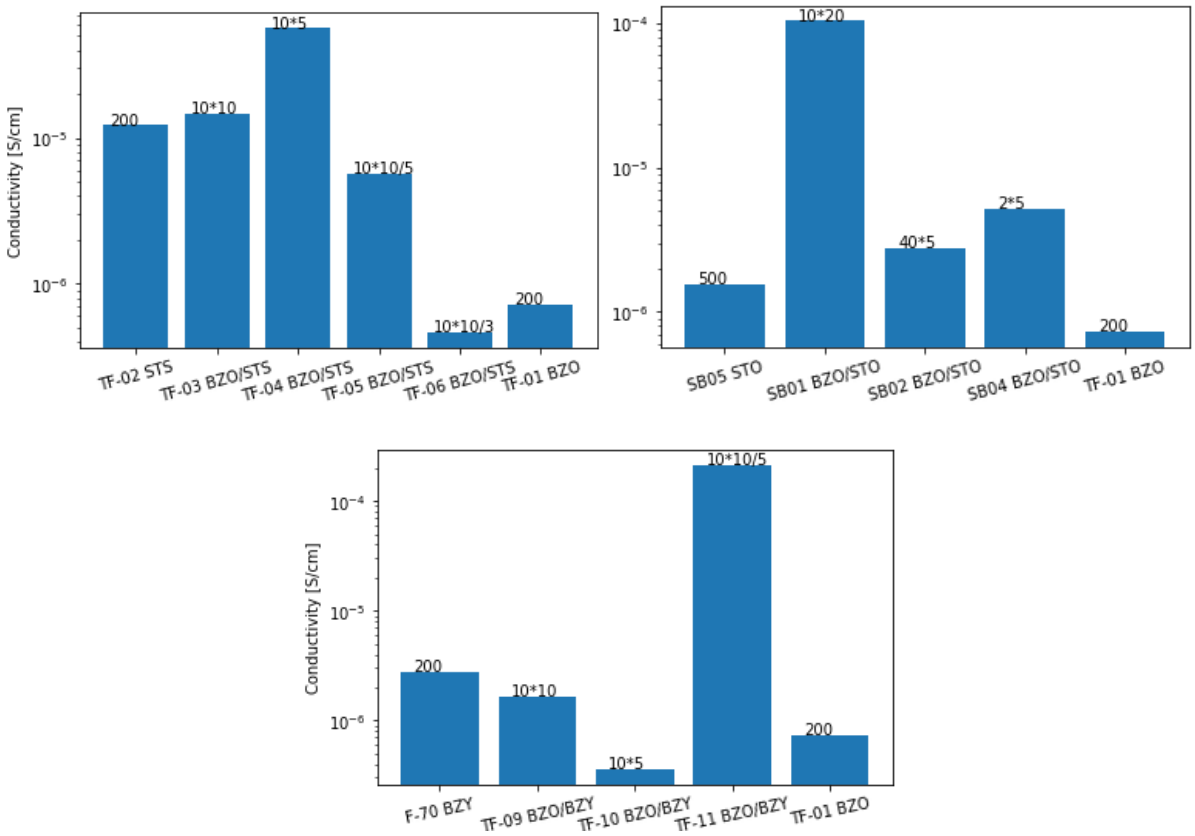

Figure 18. The conductivity of four heterostructure systems. The references are at the left at the left and right of each diagram. Some of the heterostructure films have different ratios, different thicknesses of the two materials, and are sorted accordingly. The annotations at each denote the total thickness in nm for the films, or (total number of layers) *(layer thicknesses).

Optimalization of film deposition

Deposition temperature and total film thickness were found to affect conductivity the most and the optimalization is focused on the two parameters. A comparison between the

conductivity from IS measurements of differently fabricated films is presented in (Figure 19). While there is a clear trend for the deposition temperature, there is no clear trend for the number of shots during the PLD versus conductivity (A 8). The 60 nm thick films deposited at 750 ℃ have a conductivity of approximately two orders of magnitude higher than the 1 μm thick films deposited at 600 ℃.

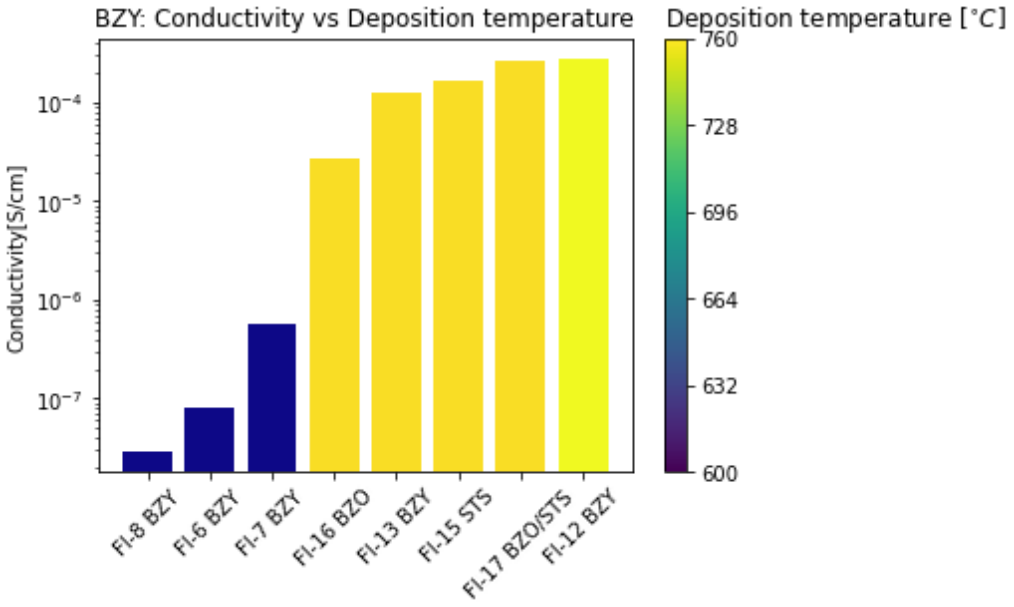

Figure 19. Conductivity versus deposition temperature of films deposited in this work. All films measured have identical thermal histories and are measured at 450 ℃ in a humid Ar atmosphere.

Temperature dependency

The temperature dependency of the conductivity was measured at 50 ℃ intervals, only two hours were allowed for ramping and equilibration, except when left overnight. As a result of the short equilibration time the defect concentrations were not allowed to fully equilibrate.

For the BZY thin film (FI-12) the defects were frozen in at 300 ℃ and below, which is seen from the flat time dependence of the conductivity after the temperature ramp (Figure 20). The measurement shows a huge increase in conductivity when going down in temperature from 600 ℃, peaking at 450 ℃. This is attributed to the hydration of the sample. However, such a peak in conductivity was not found in other BZY films, where only as slight decrease in the activation energy was observed at higher temperatures.

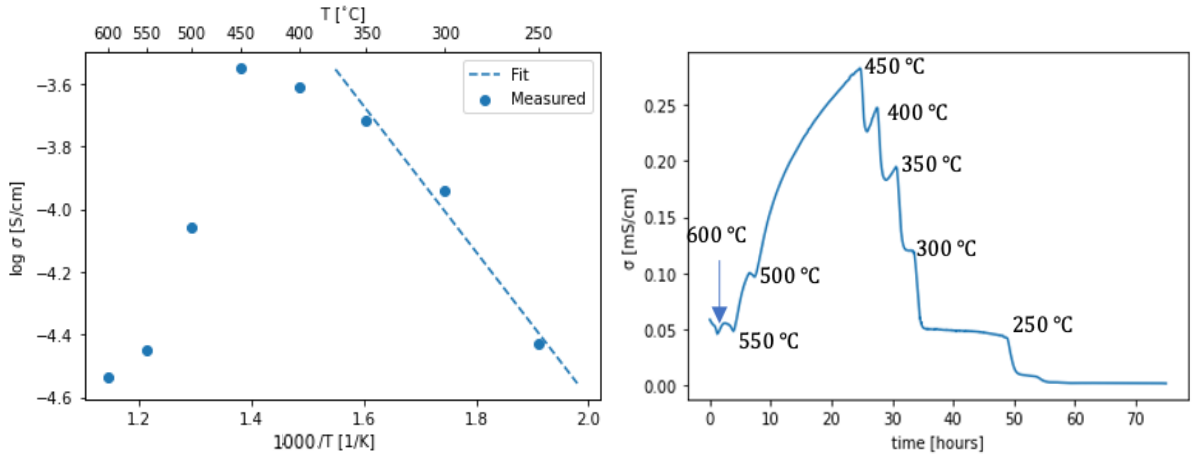

Figure 20. BZY thin film (TF-12) was measured from 600 ℃ to 250 ℃ in humid HArmix (5 % H_2) atmosphere. Left: Conductivity from deconvoluted IS, activation energy fitted from ≤ 350 ℃. Right: The constant frequency data show that the sample conductivity continues to increase after the temperature ramps above 300 ℃.

The temperature dependencies presented in Figure 21 are with the exception of the BZY film (TF-12), measured after heating to 450 ℃ and subsequent cooling. The films degraded quickly, and a conductivity decrease of 1-2 orders of magnitude was observed for the BZO, BZO/STS and STS films after said heat treatment. Therefore, the large gap in conductivities is observable between the BZY and the other films.

To investigate the BZO/STS heterostructure the materials activation energy was measured by performing impedance sweeps from 250 ℃ to 600 ℃ in humid Ar(g) atmosphere. The activation energies are listed in table of (Figure 21). All the barium zirconate containing films have an activation energy in the lower range which can be attributed to proton mobility, while the STS sample has a higher activation energy which is expected for oxide ion conduction. The BZO sample was highly resistive and only the leftmost part of the Nyquist plot semicircle was usable because of high noise at low temperatures. Empirical data from this study has shown that deconvolution using only the leftmost high frequency region typically results in overestimated conductivities. Therefore, the activation energy of BZO was calculated for temperatures from 400 ℃, where the impedance could be properly deconvoluted.

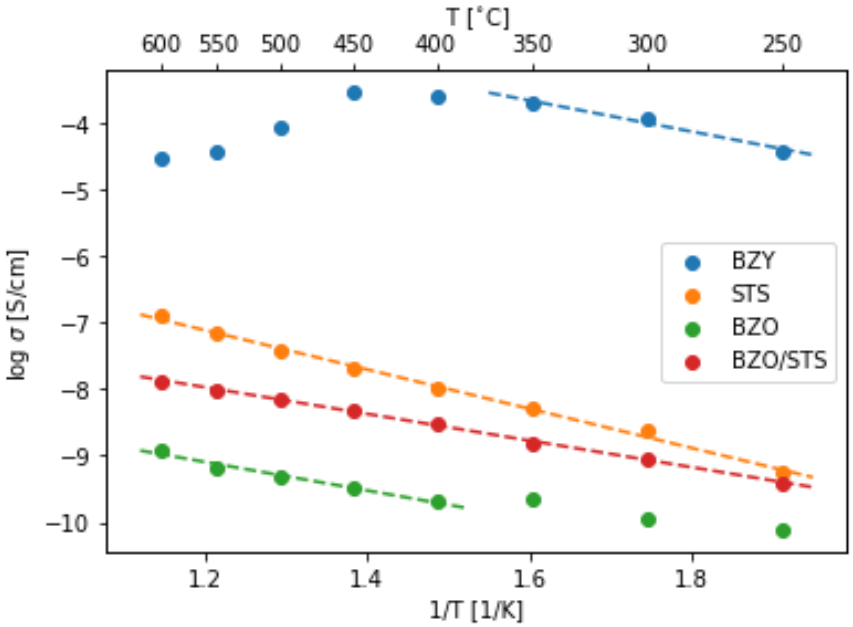

System	E_a (eV)
BZY	0.51
STS	0.64
BZO	0.49
BZO/STS	0.45

Figure 21. Arrhenius plot of four samples. Note that the STS, BZO and BZO/STS samples have been measured at 450 ℃ prior to the temperature dependence measurement. The stippled lines illustrate the temperature range of which the activation energy was calculated, and the activation energies are listed in the table.

Atmosphere dependency

The defect structure of barium zirconate is dominated by protons under most pO_2 conditions as long as a humid atmosphere is maintained. STS has a hole conductivity of comparable magnitude to the proton conductivity of BZY. It is helpful and also necessary to minimize the parasitic hole conductivity contribution in the BZO/STS heterostructure as the goal is to measure whether there is a proton concentration increase in the BZO layer. Choosing a pO_2 which favours low hole concentrations in STS is therefore important. The STS conductivity as a function of pO_2 is shown in (Figure 22). The pO_2 is assumed to be in the range where the hole concentrations increase with the pO_2 while the H^+ and O^{2-} concentrations remain constant (Figure 2). At the pO_2 range both ionic and holes contribute to the conductivity, giving as flatter slope in Figure 22 (0.143) compared to the theoretical slope expected for a hole conduction mechanism (0.25).

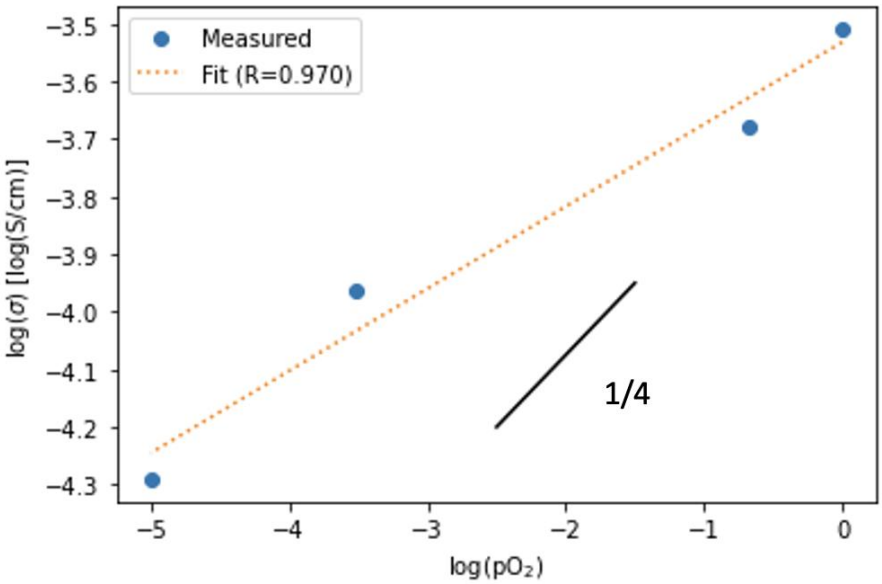

Figure 22. The pO2 dependence of a STS thin film (TF-2) measured at 600 ℃ under dry conditions. The fit gradient is 0.143. Lower than the theoretical value of ¼ for electron hole dependency from the Brower diagrams.

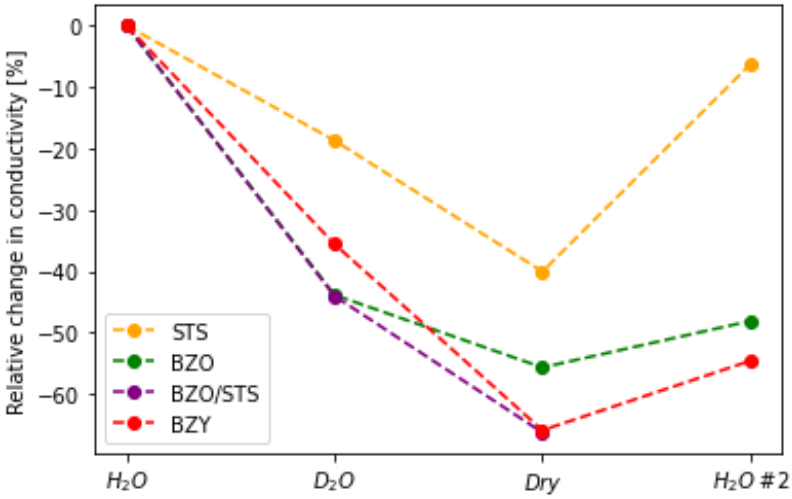

Figure 23. Water vapor dependency of four films at 450 ℃. The measurements were performed from left to right and the first measurements in H_2O is set as the reference value.

The water vapor dependency of the conductivity of the samples was measured at 450 ℃ using Ar as a carrier gas (Figure 23). As the films had a large difference in preexponential factors it was best to plot the relative change in conductivity, instead of absolute conductivity. All the films show a substantial drop in conductivity from H_2O to D_2O indicating that protons are the primary charge carrier for the barium zirconate containing films. From 40 to 65 % of the conductivity is retained when going from humid to dry conditions. The conductivity in dry conditions might be attributed to holes or oxygen vacancies. The BZO/STS exhibits a stronger water vapor dependency than both the STS and BZO reference films, indicating that

the heterostructure might positively enhances the proton conduction. The BZO and BZY films seem to degrade significantly when going to dry conditions and back to wet. Slight degradation is measured over time for the films, however not as pronounced as measured for the pH_2O switch.

Other measurements

The parallel capacitance of the thin films (uncorrected for geometry) was found to be approximately equal to the capacitance of the naked MgO substrate, around 10^{-12} Fcm^{-1}. Which is in the range of bulk processes; the value only reflects the capacitance of the substrate and not the films, however. As the substrate is much thicker than the thin film it therefore dominates the capacitance. The resistance of the square MgO substrate was further measured to be $\sim 100\ G\Omega$. Some of the films measured have a resistance in the same range, and the measured conductivity can therefore not be solely attributed to the film.

Plots of the reactance of the films versus the frequency simply visualizes the timescale at which the different mechanisms occur (Figure 24). Typically for proton conduction in BZY the peak is found at frequencies above 10^4 Hz [11], however the optimized samples have peaks in the range from 10^2 - 10^3 Hz. The peaks of the unoptimized films are found at frequencies below 10 Hz.

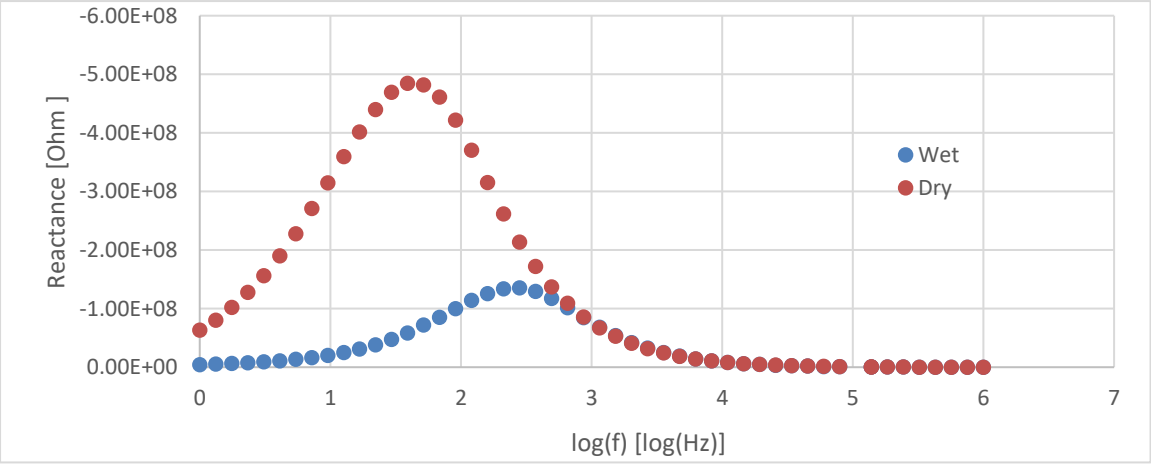

Figure 24. The reactance versus frequency of a BZY film in both dry and humid Ar atmosphere. The characteristic frequency of the dry measurement is at a significantly lower frequency than the wet.

A direct current was applied during the IS measurements to investigate if the impedance measured could be attributed to the electrode-electrolyte double layer capacitance (Figure

25). No difference in the spectra was observable, eliminating the possibility of electrode interface contributing to the impedance [50].

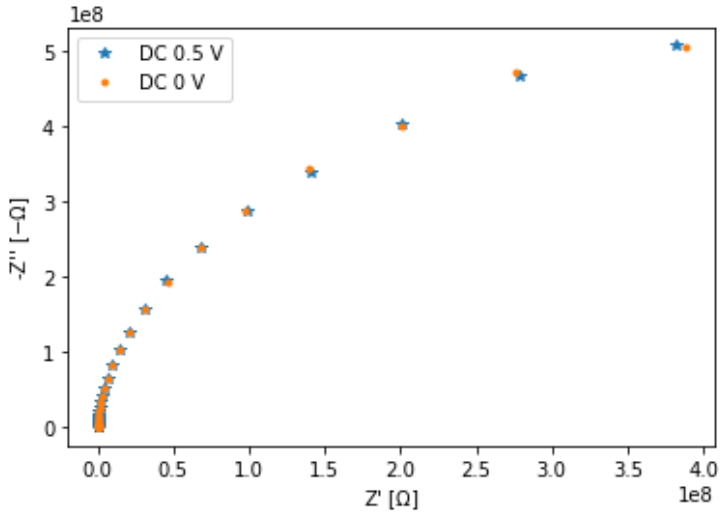

Figure 25. IS measurement comparison with and without applied DC down to 1 Hz of a BZO/STS sample (TF-17). There is no real difference between the measurements, suggesting that there is no considerable electrode polarization effect.

5.3 Computational

The $4 \times 4 \times 4$ BZY1.6 supercells (1 Y dopant per 64 unit cells) deviate slightly from the cubic symmetry. Its different lattice constants varying by $0.06\ \% - 0.16\ \%$. The trapping energy of BZY1.6 has been calculated for different degrees of compressive and tensile biaxial strain ranging from 3 % to -3 %. The -3 % strained cells result in trapping energies one order magnitude higher than the others and are therefore omitted. The calculated out-of-plane strain has an opposite sign around half the absolute value of the in-plane strain. The values can be read from (Figure 26).

Static and dynamic cell volume

The trapping energies calculated from equation (64) are presented in (Figure 26). The calculations using identical cell volumes for each strain level result in a linear relationship. In contrast to the supercells with a dynamic volume which show a parabolic relationship between the trapping energy and strain. Both models predict a trapping energy decrease for tensile strain. However, for the static cell volume calculations negative trapping energies, a repulsive force is predicted for an in-plane strain from 2 %. Under compressive strain the two models predict the opposite effects.

Relative proton-yttrium distances

The trapping energy for the relative Y-H^+ positions is also added for comparison to (Figure 26) The relative Y- H^+ position total energies yield trapping energies in the range from 0.16 eV to 0.34 eV. The trapping energies are calculated as the difference between the most stable configuration and the furthest possible Y- H^+ distance in the supercell. The trapping energies follows the same trend as the two prior methods under tensile strain. For the compressive strain calculation, the 2NN configuration was found to more stabilizing resulting in an increase in trapping energy. Had the difference between the 1NN and "far" been used instead, the trapping energy for the compressive strain would have been lower than the non-strained cell.

The energies of the Y- and H^+-doped supercell was calculated at different proton – Yttrium distances. Their relative energies are presented in (Figure 27). A slight decrease in the trapping energy can be seen for the 1 % and 3 % tensile strained cells while the compressive strain results in an increased trapping energy. The trapping energy also presents a substantial barrier energy at the R2NN site (the 2NN oxide ion site with proton rotated 90 ° away from Y), which increases with increasing tensile strain. One 2NN supercell at 0 % strain was calculated by relaxing volumetrically (Figure 26, blue dot), giving an slightly lower energy than the 1NN site in agreement with literature [65].

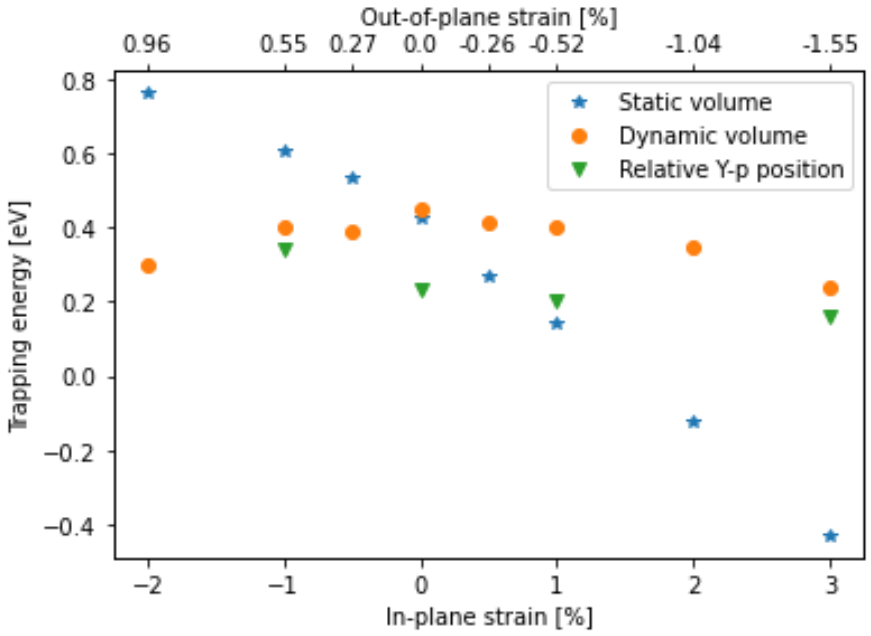

Figure 26. The trapping energies as a function of strain. The trapping energies for the relative Y-H^+ positions are calculated as the difference between the most favourable configuration, either 1NN or 2NN, and the "far" position.

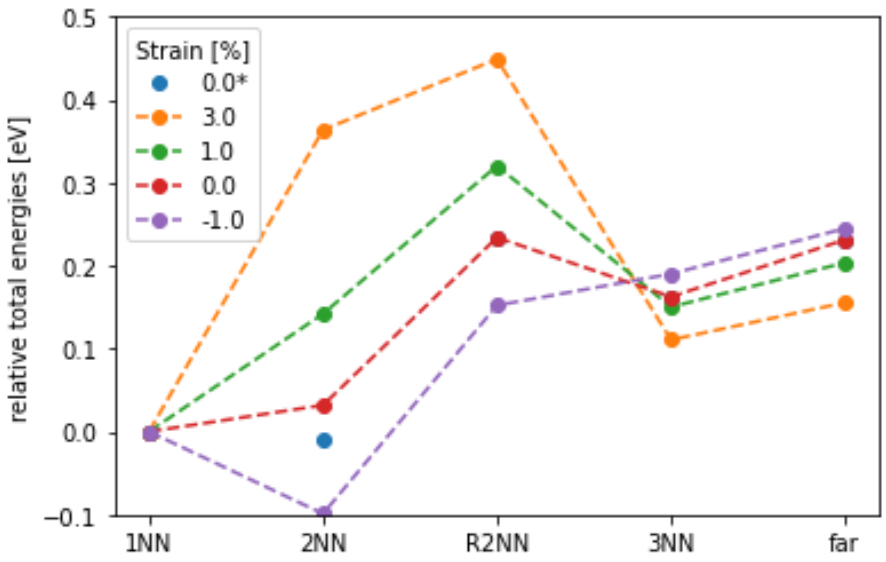

Figure 27. The relative energy of differently strained cells. * Represents a 2NN supercell which has been relaxed volumetrically, resulting in a total energy decrease of $\sim -0.04\ eV$ compared to the 1NN site. The strain given in the legend is the biaxial lattice strain in the ab-plane.

Hydration energies

The hydration enthalpy of $BaZrO_3$ was found to be -64 kJ/mol when relaxing each of the differently doped supercells volume-wise. When restraining the supercell volumes of the doped cells to be equal to the perfect supercell, a hydration enthalpy of -69 kJ/mol is calculated. Hydration energies were calculated according to equation (66).

6 Discussion

6.1 Heterostructure

Optimalization

The thin films (60 nm) deposited at 750 ℃ achieved the highest conductivities and resulted in good reproducibility (Figure 19). The conductivity increase from the thickness reduction agrees well with the work of Shim et al. where they observe a similar trend in conductivity versus film thickness [44]. The thinner films are characterized by an absence of the (110) reflection in the XRD diffractogram (Figure 16). In fact, only the reflections of planes parallel with the film are visible in the diffractogram. Therefore, they cannot contain grains as the grains would create a tilting of the lattice which in turn would make new reflection planes visible in the XRD diffractogram. This is the case for the thick films where the (110) reflection and also the (111) reflections for some are visible. However, the two peaks have lower relative intensity compared to the polycrystalline pellet. This indicates that the thick films don't have a fully randomized lattice orientation and have some degree of epitaxial growth.

The conductivity of the films could probably have been improved by increasing the substrate temperature further. Empirical studies of BZY film conductivity versus substrate temperature during deposition suggest intermediate temperatures (600 ℃) give the best results [11]. In this work however, higher temperatures from 750 ℃ clearly improve film conductivities, presumably because the removal of surface groups at the MgO surface. No study of the substrate temperature range above 750 ℃ was performed and it is therefore uncertain whether there still remain surface groups after heating to 750 ℃. Two wet washing procedures were performed, detergent→isopropanol→acetone [55] and acetic acid only, followed by heating at 600 ℃ and 750 ℃ respectively. Both methods had a measured conductivity in a similar range compared to unwashed films. Suggesting that the washing methods don't significantly assist in the removal of surface groups or that new groups form in the short timeframe between the substrate washing and deposition.

Grain growth

No two separated semicircles have been observed in this work or literature for epitaxially grown thin films on a MgO substrate, as is observed for polycrystalline pellets of BZY [32]. The IS measurements however show a correlation between poor film conductivity and a more depressed semicircle in the Nyquist plot (A 4). Therefore, reducing the formation of grain boundaries is essential in order to develop highly conductive thin films. IS measurements of polycrystalline BZY samples at low temperatures typically have two separate bulk and gb semicircles when measuring at low temperatures [47]. It is assumed that the microstructure of the grains of the films versus the grains of the pellets somehow vary. Likely the grains and dislocations of the films do not result in large separations. The epitaxial film growth method originally should result in a 100 % theoretical density, not allowing for large grain separations. Assuming some epitaxial growth for the polycrystalline films, the grains might have quite similar orientations which might aid in reducing the separation of the grains and oxygen vacancy formation. These factors might make the gb of the films more similar to the bulk, perhaps explaining why only a depresses bulk semicircle and no gb semicircle is observed.

Contradicting the trend of increasing conductivity with decreasing thickness is the 1 μm BZY film (TF-12) which achieved the highest conductivity of all BZY films of this work (Figure 19). XRD analysis of the film showed no intensity at the (110) reflection, the contrary to all the other thick films. Pergolesi et al. achieved similar results in their work in the sense that the thick films reached the highest conductivity [11]. Their BZY films however reach conductivities two orders of magnitude higher than in this work.

The BZY films in this work have a measured conductivity of around two orders of magnitude lower than the reference values from literature in the temperature range from 250 ℃ to 450 ℃ [11, 44]. They measure a resistivity increase up to 10^4 - 10^6 for polycrystalline samples, similar to the resistivity measured for the lowest conductivity BZY films of this work. Shim et al. [44] assume nanograins to be the reason for the low conductivity of the thick films and assume the thinner films to be single crystalline. The optimized films show no sign of being polycrystalline from the XRD and SEM characterization (Figure 15,Figure 16). Therefore, there might be grains present in the films which are not tilted with respect to the cube on cube orientation or perhaps columnar dislocations as observed by Mi et al. [53].

Unoptimized BZY films showed three to four order of magnitude higher resistances compared to optimized films. Their activation energies were high ranging from 0.7 eV to 0.9

eV from IS measurements at 500 ℃ and below. Indicating a high energy barrier blocking the long-range charge carrier transport. The films show a drop in conductivity when measuring in D_2O and dry conditions compared to H_2O, meaning protons are the dominant charge carrier. Therefore, the high activation energy is attributed to grain boundaries and not hole or oxygen vacancy conduction. Optimized films have a high conductivity and show a near perfect semicircle which means that there is little spread of time constants and thus only the bulk resistance is represented by the semicircle. The optimized BZO and BZY containing films also have a low activation energy (Figure 21), close to the values measured from low temperature IS measurements of polycrystalline samples [7].

Degradation

The samples show a strong hydrogen isotope effect (Figure 23), confirming the proton conduction. A 66 % conductivity decrease is measured when switching to a dry atmosphere for BZY, however only a small increase of 11 % is seen when returning to wet conditions. The asymmetrical behaviour might be a result of degradation during dehydration and hydration of the film. As the oxide ion is larger than the hydroxide ion a large change in their concentrations might stress the lattice and create e.g., resistive grains.

There are several variations in the manner the films degrade with regard to the Nyquist plot. After changing the pH_2O from wet to dry and back to wet again, the films typically retain the semicircle shape, only a bigger one, meaning a higher impedance. Remeasuring a film after cooling often results in enormous impedance increase in the low frequency regime. Both behaviours might be attributed to an increased gb resistance as mentioned. Additionally, some films show large resistances in combination with high noise in at low frequencies, the latter might be attributed to worsened electrode contacting. Such electrodes often detached from their electrolyte films when disassembling the measurement setup.

Heterostructure effect

The BZO/STS heterostructure thin film (FI-17) show slightly enhanced conductivity compared to the single-phase STS and BZO films and similar conductivity to the BZY film. As STS readily conducts oxide ion vacancies, electrons and holes the proton transport number of the BZO/STS film can be expected to be lower than the BZY. However, the water vapor dependency and isotope exchange of STS was measured to be significant, about half of

what was measured for BZY (Figure 23). Meaning that a sizable part of the STS conductivity probably comes from proton transport. The pO_2 versus conductivity measurements of this work show a large conductivity increase in high pO_2. Literature also reports increased conductivity in reducing atmosphere. The high conductivities in oxidizing and reducing conditions come from an increase in holes and electrons respectively (Figure 2). The high pH_2O dependence of the STS conductivity might in addition to the proton transport by the Grotthuss mechanism, be a result of a vehicle mechanism. Due to the high concentration and conductivity of oxygen vacancies in STS as shown in literature [42], hydroxide transport might be contributing to the conductivity.

The BZO/STS heterostructure film has the highest isotope effect of all measured systems, and a similar conductivity drop in dry atmosphere compared to BZY. These results point towards BZO/STS being mainly a proton conductor. However, the conductivity decrease during the isotope and water vapor atmosphere changes for the BZO/STS might also be a result of film degradation.

While STS has a high activation energy of 0.64 eV which can be expected for oxide ion vacancy transport (Figure 21). The pure BZY and BZO films have a measured activation energy of 0.51 and 0.49 eV respectively, slightly higher than reported bulk conductivities of BZY. The BZO/STS has the lowest activation energy of 0.45 eV which is attributed to the protons migrating through the low activation barriers of the BZO layers, free of trapping sites. The proton trapping sites around Y leads to the higher activation energy in BZY. The activation energy of the BZO/STS film is similar to the energy of the BZY and BZO films which further indicates that the BZO layer of the heterostructure is the conductive layer and protons the charge carrier. Due to the low temperature measurements of the temperature dependency of BZO being inaccurate, the activation energy at lower temperatures might actually be higher because of trap free conduction and dehydration at higher temperatures, as discussed earlier. However, BZO and STS reference films with identical thermal history show a linear dependence and no change in activation energy over the measured temperature range. It is therefore plausible that the BZO/STS film similarly has a linear temperature dependency.

Assuming that the STS layers of the heterostructure film has the same conductivity as the single-phase STS film, the conductivity of the BZO in the heterostructure is found by

assuming that the conductivity of the heterostructure film is an average of the two constituent materials:

$$\sigma_{BZO,h} = 2\sigma_{BZO/STS} - \sigma_{STS,sp} = 0.37\ mScm^{-1} \quad (67)$$

Where the subscripts *h* and *sp* denote the conductivity of the materials in the heterostructure and single-phase film respectively. The approximated conductivity is slightly higher than any other conductivity measured for BZY in this work ($0.28\ mScm^{-1}$).

The work of Mi et al. [53] showed that the BZO/STO interface has a high density of dislocations. Such dislocations are detrimental to ionic transport and should decrease the conductivity of the heterostructure compared to the reference films. As the STO is undoped its proton and oxygen vacancy concentrations should be low, and the transport of the charge carriers over to the BZO layer should be negligible. However, a conductivity increase is measured for the BZO/STO heterostructure compared to the reference films. A possible explanation simply is that the space-charge effect enhances the BZO proton concentration. Perhaps the dislocations are concentrated along the interfaces such that the interior of the highly conductive layers are unaffected. The protonic transport which is measured parallel to the planes could as such be unaffected by the dislocations as the protons mainly move in the BZO layer, circumventing the dislocations.

Transport number

The transport number of the BZY films most probably is dominated by proton conduction in wet Ar atmosphere. This is confirmed through the via the isotope exchange, both a decrease in conductivity and activation energy increase of 0.02 eV is observed when measuring the conductivity of deuterium compared to protons. A slight pO_2 dependence of the BZY conductivity can be seen (A 5). The conductivity increases with increasing pO_2, suggesting that there is some parasitic hole conductivity contribution. An increase in conductivity is also observed when switching to a reducing HArmix (A 6). Switching from humid Ar to a humid HArmix is assumed to increase the conductivity following equations (5) and (8), increasing both electron and proton concentrations. Whether the observed increase in conductivity is because of an increase in concentrations of protons, or protons and electrons is uncertain and depends on the ratio between holes and electrons in under the inert conditions. As protons are assumed to be the dominating charge carrier concentration wise, a decrease in pO_2 can affect

the hole/electron ratio in two ways (Figure 2). Either the hole concentration and total electron and hole concentration decreases, or the electron concentration increases also increasing the hole and electron concentration.

The measured BZO thin film (FI-16) conducts well as it should only have intrinsic defects given its nominal stoichiometry. However, during sintering of the pellets at high temperatures (1600 ℃) it is common that some of the volatile barium escapes. Which leads to a cation under stoichiometry which must be charge compensated by positive defects such as protons or oxygen vacancies.

The space charge effect on the heterostructure

The space charge layer around the BZO/STS interface can be expected to behave similarly as the BZY/STS interface as calculated by Saeed et al. (Figure 11). The hydration enthalpies of BZO are assumed to be somewhat lower than for BZY due to the absence of the Y- H^+ association energy. Meaning that the protons and oxide ion vacancies will segregate to the BZO layer from the STO to a slightly lesser degree than for the acceptor doped STS/BZY system. As the BZO layer experiences an increase in positive defect concentrations the STS layer must experience an equivalent decrease, and the conductivity of the BZO layer might therefore be higher than the gross approximation of equation (67). Assuming that the heterostructure system does not alter the total concentration of mobile charge carriers compared to the reference films.

The metal electrode/electrolyte interface was investigated by applying a small DC voltage (0.5-1.0 V) and no changes were observed in the Nyquist plot. In the presence of space charge regions, the impedance spectra might change under a DC. However, measuring over such a long electrolyte with potentially a high density of nanograins with their respective space charge layers only leaves a miniscule potential drop over the metal/electrolyte space charge layer. The Ag/BZO interface was calculated by Saeed and Bjørheim to result in a net proton concentration decrease while the Pt/BZO interface results in a net proton increase in the space charge layer of BZO [21]. No change in the Nyquist plot or total conductivity was observed for the two different electrodes for the AC measurements with frequencies down to 1 Hz. Though the system used in this work is probably poorly suited to measure the space charge effect as the 2D interface offers a low surface area in addition to the electrolyte resistance being very high, overshadowing other contributions.

For the single phase layers the space charge layers are expected to not have a significant effect on the conductivity in BZY assuming them to be single crystalline. The MgO/BZY interface and the BZY surface are enriched in especially protons as calculated by Polfus et al. [74, 75]. The net positive charge at the two interfaces lead to space charge layers of up to 2 and 3 nm for the BZY interface with MgO and the surface respectively. As the interfaces aren't enriched in oxygen vacancies such as a gb, they don't decrease the proton concentration as such. But because of the large stabilization the protons experience at the interfaces they can be assumed to be immobile. The conductivity drop because of the space charge layer proton depletion is in the range of a few percentages for the 60 nm thick films.

Dehydration at high temperatures

All the films experience a drop in conductivity going from wet to dry conditions (Figure 23), however only the BZY film experiences an increase in conductivity from 600 ℃ to 450 ℃, assumed to be a result of hydration of the film. The thermal history of the BZY film was however different to the other optimized films prior to the temperature dependence measurement, as the other films had been heated to 450 ℃ in humid Ar prior. A possible explanation is that the other films than the BZY were able to hydrate before the temperature dependency measurement. When heated to 600 ℃ they don't fully dehydrate resulting in a smaller proton concentration dependency versus the temperature. The BZY film however, never having been able to hydrate prior to the temperature dependency measurement, was hydrated during the measurement, when going from high to low temperatures.

Few studies have measured the proton conductivity in thin film BZY over such a broad temperature range. Pergolesi et al. [11] report no dehydration up to 600 ℃ for his single crystalline films which is reflected in the linear dependency of their total conductivity Arrhenius plot. The Arrhenius plot of the polycrystalline film of Pornprasertsuk et al. [47] however, show a reduction of the gradient around 450 ℃. The curvature in the Arrhenius plot might be a result of a reduction in charge carrier concentration because of dehydration, removing protons. However, the curvature is also in the same temperature range where a transition from trap-dominated to free protons is expected, resulting in a lower activation energy at higher temperatures [12]. The results from literature and this work therefore shows that the temperature dependence of the BZY proton conductivity might be greatly affected by the microstructure.

6.2 Lattice strain

Performing or not performing volume relaxation for the differently structured supercells prior to straining results in different activation energy dependencies of the applied strain. As evident in (Figure 26) where opposite trapping energy effects are measured at compressive strain. The static volume calculations predict too large trapping energy changes, making the results unusable. The dynamic calculations assume the 1NN to be the trapping site. However, as the relative calculations and literature [37] show, relaxing each of the differently doped cells volumetrically the 2NN site tends to become the most stable Y- H^+ configuration for a strain below zero. Therefore, the dynamic calculations in the compressive range must be treated critically. The relative Y- H^+ calculations trapping energies might be slightly underestimated as the energies are not treated from an infinite distance, but at a Y- H^+ distance of ~11.2 Å.

Experimental evidence from Fluri et al. [1] indicates that the activation energy follows a linear relationship, decreasing with increasing tensile strain. The activation energy decrease is around 0.07 eV from -0.3 % to 0.7 % strain. Which is in the range calculated by the relative Y-p position calculations. The experimental data of Fluri et al. agree surprisingly well with the relative Y-H^+ position computations of this work, showing a stronger trapping energy dependence at compressive strain than tensile. Furthermore, they were unable to fabricate films with a strain lower than -0.3 % due to dislocations reducing the strain. Similarly, the large deviations of the -3 % calculations of this work indicate that high compressive strain is unfavourable for BZY.

For the unstrained and tensile strained cells, the R2NN site was found to have the highest energy. The R2NN is the same hydroxide site as the 2NN, but with the proton rotated 90 ° away from the Y-dopant. This creates a strong energy barrier associated with the trapping energy when the proton is moving away from the dopant, and only a small energy barrier when moving towards the dopant. At 1 % tensile strain the trapping energy is reduced by 0.03 eV, while the barrier height has increased by 0.09 eV. Therefore, even though tensile strain may reduce the trapping and activation energy, it may still be detrimental to long range proton transport because of the barrier energy. Fluri et al. came to a similar conclusion by performing DFT molecular dynamics calculations where they found that both compressive and tensile strain above around 0.2 % result in a reduced proton diffusivity.

Two strain dependent effects are hypothesized by Fluri et al. to affect the proton conductivity in BZY. Firstly, a jump distance related effect; for tensile in-plane strain O-O distance is increased increasing the energy for proton transfer between the oxide ions. Simultaneously, the lattice is compressed in the out-of-plane direction resulting in a shorter O-O distance and lower migration energy barrier. Secondly, there is the trapping energy dependence of the strain which only affects the BZY and not undoped BZO. In addition to the increased $Y\text{-}H^+$ distance reducing the proton transport for tensile strain, the author hypothesizes that the energy barrier from the $Y\text{-}\ H^+$ association might further decrease the long-range transport of protons under tensile strain.

A compressive strain up to 0.5 % can be expected for the BZY films deposited onto MgO calculated from the lattice constants given in (Table 1). In contrast, some other authors report higher MgO lattice constants resulting in approximately zero strain [44]. Regardless, assuming epitaxial growth without dislocations the 0.5 % compressive strain can be assumed to give a trapping energy of 0.05 eV. The strain free conductivity can be calculated for BZY from equation (24) assuming a constant preexponential factor. The result is a theoretical doubling of the conductivity by removing the detrimental compressive strain effect. Similarly, replacing the substrate layer or the STS layers of the heterostructure with a material with slightly higher lattice constant than BZY might further increase the conductivity by reducing the activation energy.

The 7 % lattice mismatch between BZY and STS results in dislocations in the interface region to reduce the stress. The degree of strain experienced by the BZO layer in the BZO/STS heterostructure film is therefore highly uncertain. Any compressive strain experienced by BZY is found to increase the trapping energy and thus potentially decrease proton conduction. However, as BZO do not have any acceptor dopant trapping sites, the compressive strain will increase the activation energy of proton transport by increasing the trapping energy. Therefore, might the compressive strain experienced by the BZO of the BZO/STS heterostructure actually aid in proton transport by reducing the O-O distances.

6.3 Further work

This work shows that a job-sharing effect where one phase acts as a donor and the other as a conductor of protons is possible. By better understanding the relation between strain and film growth, appropriate materials choices can be made. STO and BZO have a too large difference

in their lattice constants resulting in dislocation probably reducing the conductivity. Computational efforts to find a material to substitute STS, focusing on high proton segregation energy and a good lattice match is necessary to improve the perovskite heterostructure proton conductivity. Furthermore, finding materials that have a lower parasitic conductivity contribution than STS will ease characterization by IS.

Further optimization of deposition and layer thicknesses of each of the materials constituting the heterostructure should be explored to understand the potential of the job-sharing mechanism.

7 Conclusion

In the present work the defect chemistry the $BaZr_{1-x}Y_xO_3$ and $SrTi_{1-x}Sc_xO_3$ layered thin film heterostructure has been investigated. The films were fabricated by pulsed laser deposition onto single crystalline MgO substrates. Optimization of the PLD process was performed. The resulting conductivities of the $BaZr_{0.9}Y_{0.1}O_3$ films varied by four orders of magnitude for different PLD settings. XRD characterization reveal that the films favour single crystalline over polycrystalline behaviour at high temperature > 750 ℃ and for few shots/low thickness < 1800/60 nm.

Strip electrodes were applied to the films and connected to a measurement setup allowing for temperature and atmosphere control during conductivity measurements. Impedance spectroscopy measurements were performed from 1 MHz to 1 Hz while varying temperature and pO_2. The conductivity of the $BaZr_{0.9}Y_{0.1}O_3$ reference film was measured at 450 ℃ to be 0.28 mS/cm in humid Ar. The $BaZrO_3/SrTi_{0.9}Sc_{0.1}O_3$ heterostructure film had a comparable conductivity of 0.27 mS/cm. The hydrogen isotope exchanges of the reference and heterostructure film resulted in similar conductivity dependencies, and the wet to dry atmosphere switch resulted in a 65 % conductivity decrease for both films.

The temperature dependency of the conductivities was measured from 600 ℃ to 250 ℃, giving an activation energy of 0.45 eV for the $BaZrO_3/SrTi_{0.9}Sc_{0.1}O_3$ heterostructure film. The $BaZrO_3$ and $SrTi_{0.9}Sc_{0.1}O_3$ reference films had an activation energy of 0.49 eV and 0.64 eV respectively. No change in the activation energy was measured for the BZO, BZO/STS and STS films in the temperature range measured which indicates that no dehydration or trapping effect is affecting the films in the temperature range measured.

The effect of strain on the trapping energy was assessed by first principles calculations applying density functional theory. By adjusting the yttrium – proton relative positions in a 4 by 4 supercell of barium zirconate doped with one yttrium and one proton, the trapping energy and the energies at the four closest $Y\text{-}H^+$ distances were calculated. The trapping energies agreed with experimental values from literature [1]. For -1, 0 and 1 % in-plane strain, trapping energies of 0.34, 0.23 and 0.20 eV respectively was measured. In addition to the trapping energy, there was found to be an energy barrier associated with the second closest oxide ion – Y neighbours. The barrier might be detrimental to long range proton transport for both compressive and tensile strain.

The conductivity dependencies of the temperature and water vapor pressure point towards protons being the dominating charge carrier of the $BaZrO_3/SrTi_{0.9}Sc_{0.1}O_3$ heterostructure. The results suggest that the heterostructure engineering might improve the state-of-the-art $BaZr_{1-x}Y_xO_3$ proton conducting electrolyte material. The conductivity of the BZO of the heterostructure was calculated to increase by an order of 14 compared to the reference film. The conductivity increase is attributed to the charge carrier enrichment of the BZO by the job sharing-mechanism, where the STS layer transfers its protons and oxygen vacancies to the BZO layer. The compressive strain experienced by the BZO layer of the heterostructure is expected to result in increased proton conductivity, whereas a conductivity decrease is expected for the BZY because of an increased proton trapping.

Bibliography

1. Fluri, A., et al., *Enhanced Proton Conductivity in Y-Doped BaZrO3 via Strain Engineering.* Advanced Science, 2017. **4**(12): p. 1700467.
2. Stips, A., et al., *On the causal structure between CO2 and global temperature.* Scientific Reports, 2016. **6**(1): p. 21691.
3. IEA (2020), R.e.m.u., IEA, Paris https://www.iea.org/reports/renewable-energy-market-update.
4. Duan, C., et al., *Highly efficient reversible protonic ceramic electrochemical cells for power generation and fuel production.* Nature Energy, 2019. **4**(3): p. 230-240.
5. Fabbri, E., D. Pergolesi, and E. Traversa, *Materials challenges toward proton-conducting oxide fuel cells: a critical review.* Chemical Society Reviews, 2010. **39**(11): p. 4355-4369.
6. Norby, T., *Solid-state protonic conductors: principles, properties, progress and prospects.* Solid State Ionics, 1999. **125**(1): p. 1-11.
7. Kreuer, K.D., et al., *Proton conducting alkaline earth zirconates and titanates for high drain electrochemical applications.* Solid State Ionics, 2001. **145**(1): p. 295-306.
8. Kreuer, K.D., *On the development of proton conducting materials for technological applications.* Solid State Ionics, 1997. **97**(1): p. 1-15.
9. Kreuer, K.D., *Proton-Conducting Oxides.* Annual Review of Materials Research, 2003. **33**(1): p. 333-359.
10. Pergolesi, D., et al., *Probing the bulk ionic conductivity by thin film hetero-epitaxial engineering.* Science and technology of advanced materials, 2015. **16**(1): p. 015001-015001.
11. Pergolesi, D., et al., *High proton conduction in grain-boundary-free yttrium-doped barium zirconate films grown by pulsed laser deposition.* Nature Materials, 2010. **9**(10): p. 846-852.
12. Yamazaki, Y., et al., *Proton trapping in yttrium-doped barium zirconate.* Nature Materials, 2013. **12**(7): p. 647-651.
13. Ngabonziza, P., et al., *2D Doping of Proton Conductors: BaZrO3-Based Heterostructures.* Advanced Energy Materials, 2021. **11**(4): p. 2003267.
14. Saeed, S.W., T. Norby, and T.S. Bjørheim, *Charge-Carrier Enrichment at BaZrO3/SrTiO3 Interfaces.* The Journal of Physical Chemistry C, 2019. **123**(34): p. 20808-20816.
15. Truls Norby, Y.L., *Concentration and transport of protons in oxides.* Current Opinion in Solid State and Materials Science, 1997. **Vol: 2**(5): p. 593-599.
16. Polfus, J.M., et al., *Nitrogen defects in wide band gap oxides: defect equilibria and electronic structure from first principles calculations.* Physical Chemistry Chemical Physics, 2012. **14**(33): p. 11808-11815.
17. CJ.D. von Grotthuss, A.C.L.
18. R.D. Shannon, R.E.I.R.a.S.S.o.I.D.i.H.a.C., Acta Cryst. A32 751-767 (1976).
19. Maier, J., *Nanoionics: ion transport and electrochemical storage in confined systems.* Nature Materials, 2005. **4**(11): p. 805-815.
20. Sata, N., et al., *Mesoscopic fast ion conduction in nanometre-scale planar heterostructures.* Nature, 2000. **408**(6815): p. 946-949.
21. Saeed, S.W. and T.S. Bjørheim, *The Role of Space-Charge at Metal/Oxide Interfaces in Proton Ceramic Electrochemical Cells.* The Journal of Physical Chemistry C, 2020.

22. Polfus, J.M., et al., *Defect chemistry of a BaZrO3 Σ3 (111) grain boundary by first principles calculations and space–charge theory.* Physical Chemistry Chemical Physics, 2012. **14**(35): p. 12339-12346.
23. Wolfram Koch, M.C.H., *A Chemist's Guide to Density Functional Theory*. Second Edition ed. 2001: Copyright © 2001 Wiley-VCH Verlag GmbH.
24. Hohenberg, P. and W. Kohn, *Inhomogeneous Electron Gas.* Physical Review, 1964. **136**(3B): p. B864-B871.
25. Perdew, J.P., K. Burke, and M. Ernzerhof, *Generalized Gradient Approximation Made Simple.* Physical Review Letters, 1996. **77**(18): p. 3865-3868.
26. Csonka, G.I., et al., *Assessing the performance of recent density functionals for bulk solids.* Physical Review B, 2009. **79**(15): p. 155107.
27. T. Takahashi and H. Iwahara, R.C.M.
28. Iwahara, H., et al., *Proton conduction in sintered oxides and its application to steam electrolysis for hydrogen production.* Solid State Ionics, 1981. **3-4**: p. 359-363.
29. H. Uchida, H.Y., H. Iwahara, *Formation of protons in SrCeO3-based proton conducting oxides. Part 1.* Solid State Ionics, 1989. **34**: p. 103-110.
30. Iwahara, H., et al., *Protonic conduction in calcium, strontium and barium zirconates.* Solid State Ionics, 1993. **61**(1): p. 65-69.
31. Kreuer, K.D., *Aspects of the formation and mobility of protonic charge carriers and the stability of perovskite-type oxides.* Solid State Ionics, 1999. **125**(1): p. 285-302.
32. Bohn, H.G. and T. Schober, *Electrical Conductivity of the High-Temperature Proton Conductor BaZr0.9Y0.1O2.95.* Journal of the American Ceramic Society, 2000. **83**(4): p. 768-772.
33. Schober, T. and H.G. Bohn, *Water vapor solubility and electrochemical characterization of the high temperature proton conductor BaZr0.9Y0.1O2.95.* Solid State Ionics, 2000. **127**(3): p. 351-360.
34. Islam, M.S., et al., *Doping and defect association in AZrO3 (A = Ca, Ba) and LaMO3 (M = Sc, Ga) perovskite-type ionic conductors.* Dalton Transactions, 2004(19): p. 3061-3066.
35. Björketun, M.E., et al., *A kinetic Monte Carlo study of proton diffusion in disordered perovskite structured lattices based on first-principles calculations.* Solid State Ionics, 2005. **176**(39): p. 3035-3040.
36. Björketun, M.E., P.G. Sundell, and G. Wahnström, *Structure and thermodynamic stability of hydrogen interstitials in BaZrO3 perovskite oxide from density functional calculations.* Faraday Discussions, 2007. **134**(0): p. 247-265.
37. Björketun, M.E., P.G. Sundell, and G. Wahnström, *Effect of acceptor dopants on the proton mobility in $\mathrm{Ba}\mathrm{Zr}{\mathrm{O}}_{3}$: A density functional investigation.* Physical Review B, 2007. **76**(5): p. 054307.
38. Stokes, S.J. and M.S. Islam, *Defect chemistry and proton-dopant association in BaZrO3 and BaPrO3.* Journal of Materials Chemistry, 2010. **20**(30): p. 6258-6264.
39. Braun, A., et al., *Proton diffusivity in the BaZr0.9Y0.1O3−δ proton conductor.* Journal of Applied Electrochemistry, 2009. **39**(4): p. 471-475.
40. Karlsson, M., et al., *Using Neutron Spin−Echo To Investigate Proton Dynamics in Proton-Conducting Perovskites.* Chemistry of Materials, 2010. **22**(3): p. 740-742.
41. Takahashi, H., et al., *First-Principles Calculations for the Energetics of the Hydration Reaction of Acceptor-Doped BaZrO3.* Chemistry of Materials, 2017. **29**(4): p. 1518-1526.
42. Schie, M., R. Waser, and R.A. De Souza, *A Simulation Study of Oxygen-Vacancy Behavior in Strontium Titanate: Beyond Nearest-Neighbor Interactions.* The Journal of Physical Chemistry C, 2014. **118**(28): p. 15185-15192.

43. Münch, W., et al., *A quantum molecular dynamics study of the cubic phase of BaTiO3 and BaZrO3.* Solid State Ionics, 1997. **97**(1): p. 39-44.
44. Shim, J.H., T.M. Gür, and F.B. Prinz, *Proton conduction in thin film yttrium-doped barium zirconate.* Applied Physics Letters, 2008. **92**(25): p. 253115.
45. Steinsvik, S., Y. Larring, and T. Norby, *Hydrogen ion conduction in iron-substituted strontium titanate, SrTi1−xFexO3−x/2 (0≤x≤0.8).* Solid State Ionics, 2001. **143**(1): p. 103-116.
46. Long, D.M., et al., *Conductivity of iron-doped strontium titanate in the quenched and degraded states.* Journal of the American Ceramic Society, 2019. **102**(6): p. 3567-3577.
47. Pornprasertsuk, R., et al., *Proton conductivity of Y-doped BaZrO3: Pellets and thin films.* Solid State Sciences, 2011. **13**(7): p. 1429-1437.
48. Tao, S. and J.T.S. Irvine, *Conductivity studies of dense yttrium-doped BaZrO3 sintered at 1325°C.* Journal of Solid State Chemistry, 2007. **180**(12): p. 3493-3503.
49. Schneller, T. and T. Schober, *Chemical solution deposition prepared dense proton conducting Y-doped BaZrO3 thin films for SOFC and sensor devices.* Solid State Ionics, 2003. **164**(3): p. 131-136.
50. Shirpour, M., R. Merkle, and J. Maier, *Space charge depletion in grain boundaries of BaZrO3 proton conductors.* Solid State Ionics, 2012. **225**: p. 304-307.
51. Yamazaki, Y., R. Hernandez-Sanchez, and S.M. Haile, *Cation non-stoichiometry in yttrium-doped barium zirconate: phase behavior, microstructure, and proton conductivity.* Journal of Materials Chemistry, 2010. **20**(37): p. 8158-8166.
52. Zhao, C., et al., *Heterointerface engineering for enhancing the electrochemical performance of solid oxide cells.* Energy & Environmental Science, 2020.
53. S.B. Mi, C.L.J., M.I. Faley, U. Poppe, K. Urban, *High-resolution electron microscopy of microstructure of SrTiO3/ BaZrO3 bilayer thin films on MgO substrates.* Journal of crystal growth, 2007. **300**: p. 478-482.
54. Coustet, V. and J. Jupille, *Hydroxyl groups on oxide surfaces.* Il Nuovo Cimento D, 1997. **19**(11): p. 1657-1664.
55. Febvrier, A.L., J. Jensen, and P. Eklund, *Wet-cleaning of MgO(001): Modification of surface chemistry and effects on thin film growth investigated by x-ray photoelectron spectroscopy and time-of-flight secondary ion mass spectroscopy.* Journal of Vacuum Science & Technology A, 2017. **35**(2): p. 021407.
56. Bae, K., et al., *Influence of background oxygen pressure on film properties of pulsed laser deposited Y:BaZrO3.* Thin Solid Films, 2014. **552**: p. 24-31.
57. Yamanaka, S., et al., *Thermophysical properties of BaZrO3 and BaCeO3.* Journal of Alloys and Compounds, 2003. **359**(1): p. 109-113.
58. Hirata, K., K. Moriya, and Y. Waseda, *High temperature thermal expansion of ThO2, MgO and Y2O3 by X-ray diffraction.* Journal of Materials Science, 1977. **12**(4): p. 838-839.
59. Mitchell, R.H., A.R. Chakhmouradian, and P.M. Woodward, *Crystal chemistry of perovskite-type compounds in the tausonite-loparite series, (Sr1−2xNaxLax)TiO3.* Physics and Chemistry of Minerals, 2000. **27**(8): p. 583-589.
60. Park, J., et al., *Pulsed laser deposition of Y-doped BaZrO3 thin film as electrolyte for low temperature solid oxide fuel cells.* CIRP Annals, 2013. **62**(1): p. 563-566.
61. Magrasó, A., et al., *Optimisation of growth parameters to obtain epitaxial Y-doped BaZrO3 proton conducting thin films.* Solid State Ionics, 2018. **314**: p. 9-16.
62. Ottochian, A., et al., *Influence of isotropic and biaxial strain on proton conduction in Y-doped BaZrO3: a reactive molecular dynamics study.* Journal of Materials Chemistry A, 2014. **2**(9): p. 3127-3133.

63. Schober, T., *High-temperature proton conductors: hydrogen injection and pumping.* Ionics, 2000. **6**(5): p. 369-372.
64. Draber, F.M., et al., *Nanoscale percolation in doped BaZrO3 for high proton mobility.* Nature Materials, 2020. **19**(3): p. 338-346.
65. Torayev, A., et al., *Local Distortions and Dynamics in Hydrated Y-Doped BaZrO3.* The Journal of Physical Chemistry C, 2020. **124**(30): p. 16689-16701.
66. Blanc, F., et al., *Dynamic Nuclear Polarization NMR of Low-γ Nuclei: Structural Insights into Hydrated Yttrium-Doped BaZrO3.* The Journal of Physical Chemistry Letters, 2014. **5**(14): p. 2431-2436.
67. Bjørheim, T.S., E.A. Kotomin, and J. Maier, *Hydration entropy of BaZrO3 from first principles phonon calculations.* Journal of Materials Chemistry A, 2015. **3**(14): p. 7639-7648.
68. *ProboStatTM Manual, NORECS AS, 2018, http://www.norecs.com/work/_files/__PUBLIC_FILES__/manuals/ProboStat%20Manual.pdf*. 2018.
69. G. Kresse and J. Furthmüller, P.R.B., 11169 (1996).
70. Kresse, G. and D. Joubert, *From ultrasoft pseudopotentials to the projector augmented-wave method.* Physical Review B, 1999. **59**(3): p. 1758-1775.
71. Monkhorst, H.J. and J.D. Pack, *Special points for Brillouin-zone integrations.* Physical Review B, 1976. **13**(12): p. 5188-5192.
72. Kuwabara, A. and I. Tanaka, *First Principles Calculation of Defect Formation Energies in Sr- and Mg-Doped LaGaO3.* The Journal of Physical Chemistry B, 2004. **108**(26): p. 9168-9172.
73. Norby, T. and P.E.R. Kofstad, *Electrical Conductivity and Defect Structure of Y2O3 as a Function of Water Vapor Pressure.* Journal of the American Ceramic Society, 1984. **67**(12): p. 786-792.
74. Polfus, J.M., T. Norby, and R. Bredesen, *Proton segregation and space-charge at the BaZrO3 (0 0 1)/MgO (0 0 1) heterointerface.* Solid State Ionics, 2016. **297**: p. 77-81.
75. Polfus, J.M., et al., *Surface defect chemistry of Y-substituted and hydrated BaZrO3 with subsurface space-charge regions.* Journal of Materials Chemistry A, 2016. **4**(19): p. 7437-7444.

Appendix

A 1

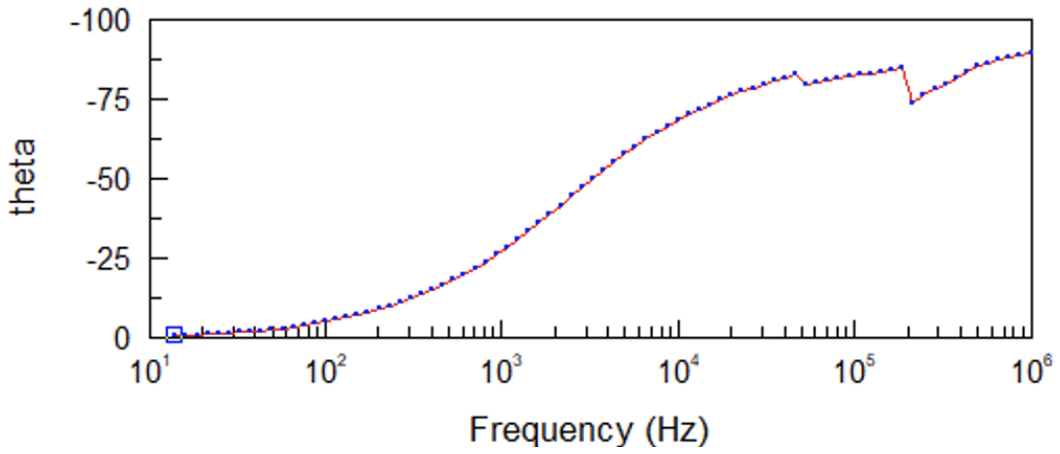

Bode plot of thin film impedance sweep. At high frequencies the impedance interface is unable to maintain a stable current, requiring it to correct the current leading errors above approximately 40 kHz. The degree of error increase with the film resistance.

A 2. Table of thin film samples included in this study**

Name	Materials	Layers
FI-1	BZY	$1 \cdot 200\ nm$
FI-2	STS/BZO	$10 \cdot 20\ nm$
FI-3	BZY	$1 \cdot 200\ nm$
FI-4	BZY20	$1 \cdot 200\ nm$
FI-5	BZY20	$1 \cdot 1\ \mu m$
FI-6	BZY	$1 \cdot 1\ \mu m$
FI-7	BZY	$1 \cdot 1\ \mu m$
FI-8	BZY	$1 \cdot 1\ \mu m$
FI-9	BZY	$1 \cdot 1\ \mu m$
FI-10	BZY	$1 \cdot 1\ \mu m$
FI-11	BZY	$1 \cdot 1\ \mu m$
FI-12	BZY	$1 \cdot 1\ \mu m$
FI-13	BZY	$1 \cdot 60\ nm$
FI-14	BZY	$1 \cdot 60\ nm$
FI.14.1	BZY	$1 \cdot 60\ nm$
FI-15	STS	$1 \cdot 60\ nm$

Name	Materials	Layers
FI-16	BZO	$1 \cdot 60\ nm$
FI-17	BZO/STS	$12 \cdot 5\ nm$
FI-18	BZO/BZY	$12 \cdot 5\ nm$
TF-01*	BZO	$1 \cdot 200\ nm$
TF-02*	STS	$1 \cdot 200\ nm$
TF-03*	BZO/STS	$10 \cdot 10\ nm$
TF-04*	BZO/STS	$10 \cdot 5\ nm$
TF-05*	BZO/STS	$10 \cdot 10/5\ nm$
TF-06*	BZO/STS	$10 \cdot 10/3\ nm$
TF-09*	BZO/BZY	$10 \cdot 10\ nm$
TF-10*	BZO/BZY	$10 \cdot 5\ nm$
TF-11*	BZO/BZY	$10 \cdot 10/5\ nm$
F-70*	BZY	$1 \cdot 200\ nm$
F-84*	BZY	-
SB01*	BZO/STO	$20 \cdot 10\ nm$
SB02*	BZO/STO	$40 \cdot 5\ nm$
SB04*	BZO/STO	$2 \cdot 5\ nm$
SB05*	STO	$1 \cdot 500\ nm$
CB01*	BZO/CGO	$20 \cdot 10\ nm$
CB03*	BZO	$1 \cdot 500\ nm$
CB05*	BZO/CGO	$4 \cdot 5\ nm$

* Films were deposited by Dr Saeed in the period from 2017 to 2018.

** All films are deposited on (001) MgO. For multilayer films the material at the left of the backslash was deposited first, directly onto the MgO surface.

A 3

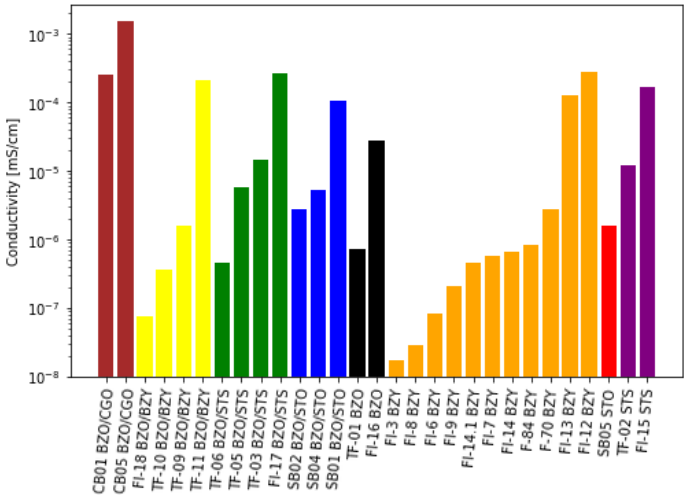

Comparison of all films measured at 450 ℃ in humid Ar. The graph shows the large variation in film conductivity.

A 4

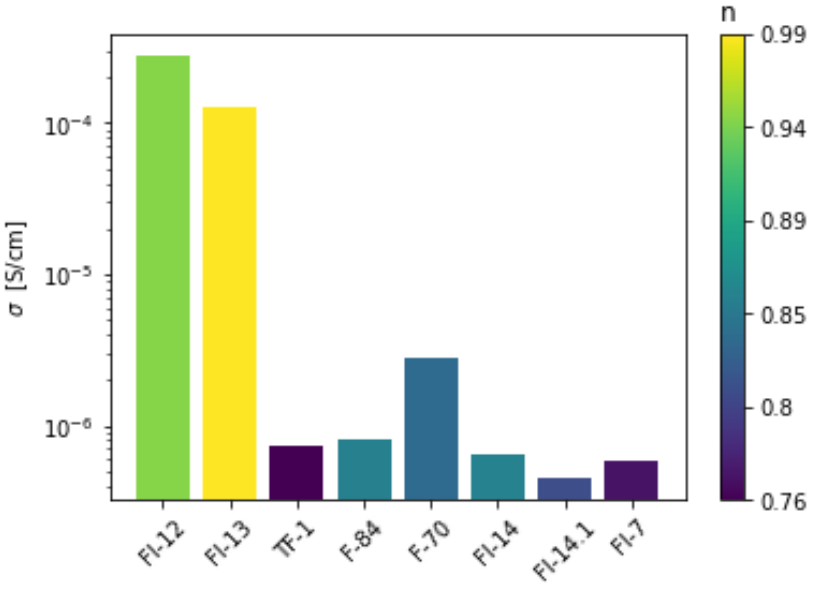

The conductivity of different BZY films, colour coded according to their *n* factor from CPE equation (35). A *n* equal to 1 yields a perfect Nyquist plot semicircle for which one might assume a unsignificant gb contribution. Or more accurately, there's no dispersion of time constant. The gb contribution is assumed to increase with decreasing *n*.

A 5

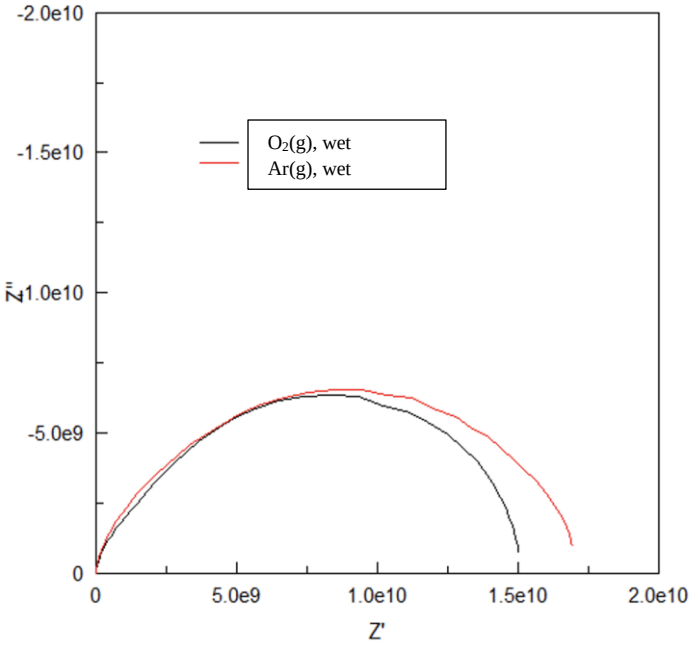

The pO_2 dependence of a BZY film (FI-8). The decrease of resistance with increasing pO_2 is attributed to an increase of holes following equation (6). The shift to higher oxygen partial pressures resulted in a 25 % increase in conductivity.

A 6

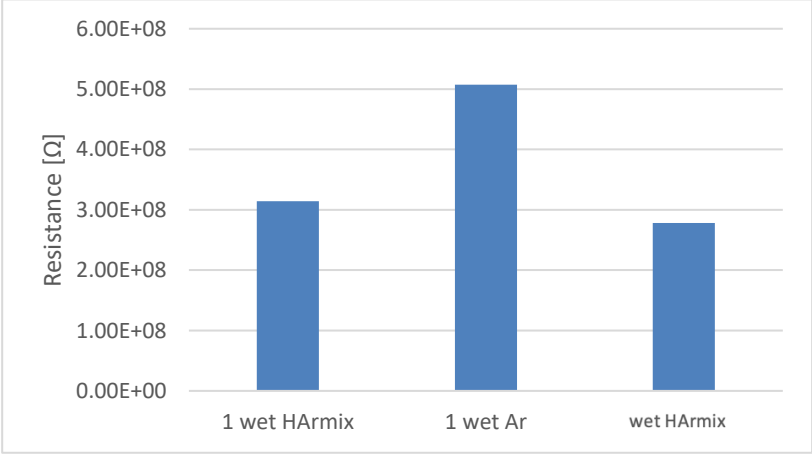

The resistance of a BZY film (FI-12) at 450 ℃ measured in humid reducing HArmix and inert Ar atmosphere.

A 7

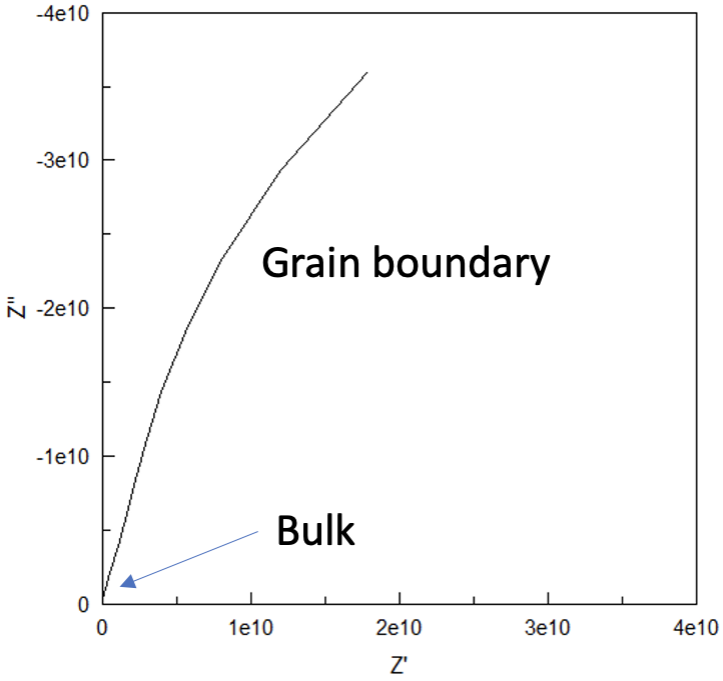

The Nyquist plot of a highly resistive BZY sample which is assumed to be dominated by gb resistance. On the left most part of the graph a slight curvature which might be assigned to the bulk resistance. The measurement is at 450 ℃ in humid Ar atmosphere.

A 8

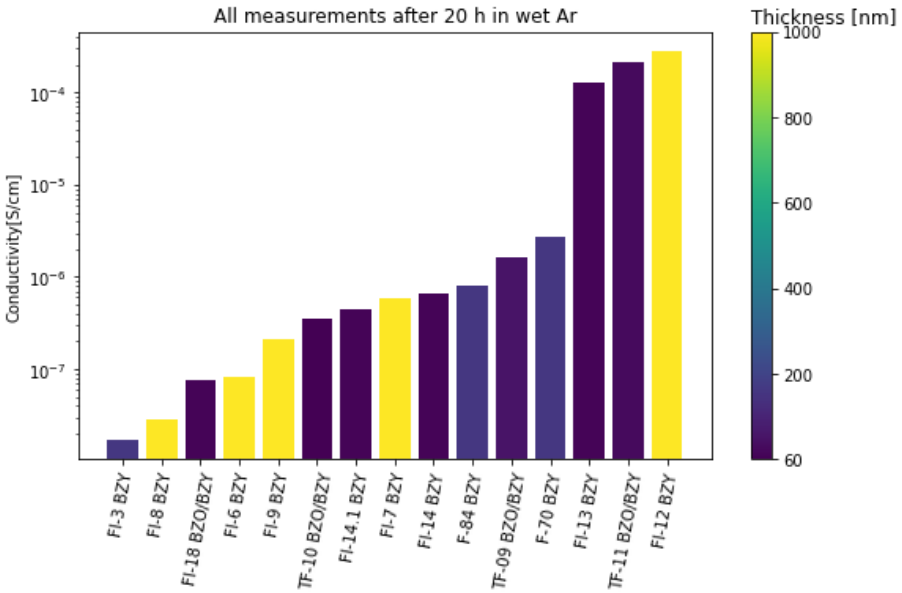

Figure 28. Plots showing the conductivity BZO and BZY films versus thickness. The films are fabricated by Dr Saeed and in this work.

A 9. VASP input files

INCAR file for relaxation of the structures:

```
!Functional

GGA = PS          !Perdew Burke Ernzehof revised for solids

! Electronic relaxation
ALGO   = Normal    ! Algorithm for electronic relaxation
NELMIN = 4         ! Minimum # of electronic steps
EDIFF  = 1E-5      ! Accuracy for electronic ground state
ENCUT  = 550       ! Cut-off energy for plane wave expansion
PREC   = Accurate  ! Precision Normal/Accurate
LREAL  = Auto      ! Projection in reciprocal space
ISMEAR = 0         ! Smearing of partial occupancies.
SIGMA  = 0.05      ! Smearing width
ISPIN  = 1         ! Spin polarization
NELECT = 2560.0         ! Number of electrons(For singly doped cells)

! Ionic relaxation
EDIFFG = -0.01     ! Tolerance for ions
NSW    = 80        ! Max # of ionic steps
MAXMIX = 80        ! Keep dielectric function between ionic movements
IBRION = 1         ! Algorithm for ions. 0: MD 1: QN/DIIS 2: CG
ISIF   = 2         ! Relaxation. 2: ions 3: ions+cell
ADDGRID= .TRUE.    ! More accurate forces with PAW

! Output options
NWRITE = 1         ! Write electronic convergence at first step only
! Memory handling
NCORE   = 2
KPAR    = 2
```

INCAR file for total energy calculation:

```
   ENCUT  = 550              ! eV energy cut-off for the calculation
PREC   = Normal     ! Normal precision
LREAL  = Auto       ! Real space projection .FALSE. or Auto
ISMEAR=-5                 ! Smearing of partial occupancies.
GGA=PS              ! Functional
NCORE = 2                 ! Memory handling
KPAR=2
   NELECT = 2560.0  ! Number of electrons(For singly doped cells)
```